Title: Conserved cellular architecture and developmental mechanisms of the zebrafish meninges

Authors:

Ashley L. Arancio[1], Kathryn Wilhem[1], Hung-Jhen Chen[1], Brandon M. Hernandez[1], Percy J. Raggi[1], D'Juan T. Farmer[1,2]

[1]Department of Molecular, Cell and Developmental Biology, University of California, Los Angeles

[2]Howard Hughes Medical Institute

Abstract

The meninges are a multilayered connective tissue that supports and protects the brain and skull, yet their developmental origins and signaling functions remain poorly understood. Here, we establish zebrafish as a tractable model for defining meningeal development and function across larval and adult stages. Using a restricted *foxc1b*:Gal4 reporter, we resolve the spatiotemporal emergence of meningeal fibroblasts and demonstrate a conserved, dosage-sensitive requirement for Foxc1 activity during meningeal formation. A targeted pharmacological screen identifies Wnt signaling as essential for timely establishment of the primary meninx. To define adult meningeal diversity, we integrate single-cell multiome profiling with spatial validation and identify multiple transcriptionally distinct populations organized into layered compartments, including pial, arachnoid, dural, and periosteal dura fibroblasts. Finally, inducible larval ablation of meningeal cells reveals limited regenerative capacity following widespread loss and leads to persistent defects in calvarial osteogenesis and brain architecture, including reduced osteoblast differentiation at bone fronts and disrupted tissue organization at sites lacking meningeal recovery. Together, these findings define key features of zebrafish meninges and provide a framework for dissecting meningeal development, regeneration, and meninges-dependent signaling in vivo.

Keywords

zebrafish, meninges, intratissue communication, craniofacial skeleton,

Summary Statement

This study uses zebrafish to show how the tissues surrounding the brain develop early and guide proper formation of both the brain and skull.

Introduction

The meninges are a multilayered connective tissue that encase the central nervous system and, in the head, lie between the brain and the skull. They are comprised of transcriptionally distinct fibroblast populations, with resident immune cells and an extensive vasculature that support tissue nourishment and waste removal (Dasgupta and Jeong, 2019; Decimo et al., 2012; O'Rahilly and Muller, 1986). Meningeal fibroblasts are broadly organized into three layers: the pia mater, which lies adjacent to the brain and is separated from neural tissue by a basement membrane; the arachnoid mater, which contributes to cerebrospinal fluid regulation; and the dura mater, which anchors the meninges to the overlying skull.

Recent single-cell sequencing studies have begun to resolve the cellular composition of embryonic and adult mouse and human meninges (DeSisto et al., 2020; Ebert et al., 2025; Kearns et al., 2023; Pietila et al., 2023). These analyses reveal substantial fibroblast heterogeneity by embryonic day 14 (E14) and extensive diversity within both the leptomeninges (pia and arachnoid) and the dura mater. Within the dura, transcriptionally distinct inner and outer (periosteal) layers have been identified. These studies highlight an unexpected degree of cellular complexity within vertebrate meninges.

Beyond their structural role, the meninges play essential functions during development by regulating neighboring tissues such as the brain and the skull (Como et al., 2023; Dasgupta and Jeong, 2019). Meningeal-derived retinoic acid signaling modulates cortical neurogenesis (Como et al., 2025; Haushalter et al., 2017; Matrongolo et al., 2023; Mishra et al., 2016; Siegenthaler et al., 2009). Signaling cues including TGFβ family ligands (Greenwald et al., 2000; Slater et al., 2009) from meninges have also been shown to influence cranial suture maintenance and calvarial growth (Cooper et al., 2012; Greenwald et al., 2000; Kwan et al., 2008; Opperman et al., 1993; Slater et al., 2008). Despite these roles, the mechanisms governing meningeal development remain incompletely understood. The forkhead box transcription factor FOXC1 is required for meningeal formation in mice and humans, as hypomorphic or null alleles disrupt meningeal development (Aldinger et al., 2009; Siegenthaler et al., 2009; Zarbalis et al., 2007). Similarly, ZIC family transcription factors are required for meningeal development, as Zic1/3 double mutants exhibit basement membrane defects and impaired fibroblast proliferation (Inoue et al., 2008). In both contexts, genetic perturbations broadly affect all meningeal layers, and only recently have

studies begun to resolve how distinct meningeal cell types are specified during development (Derk et al., 2023).

Although most functional studies of the meninges have focused on rodent models, ultrastructural analyses reveal stratified meningeal layers across vertebrate and invertebrate species, suggesting deep evolutionary conservation (Kappers, 1925; Nakao, 1979). Recent work has shown that zebrafish possess stratified meninges containing vasculature and immune cell populations comparable to those of mammals (Galanternik et al., 2025). These findings highlight zebrafish as a promising system for studying meningeal development, yet the relationships between zebrafish and mammalian meningeal layers, the transcriptional diversity of zebrafish meningeal fibroblasts, and the conservation of meningeal signaling functions remain unresolved.

Here, we define the developmental timing and molecular identities of meningeal fibroblasts in zebrafish. Using *foxc1a* and *foxc1b* mutant alleles, we demonstrate a conserved, dosage-sensitive requirement for FOXC1 during meningeal formation, with region-specific sensitivity to gene dosage. Pharmacological perturbation identifies Wnt signaling as essential for timely establishment of the embryonic meninx. Single-cell genomics resolves multiple transcriptionally distinct meningeal layers with clear parallels to murine populations. Finally, larval ablation of meninges reveals limited regenerative capacity following large-scale loss and uncovers persistent defects in both brain and skull development. Together, these findings establish zebrafish as a powerful model for dissecting the developmental and regulatory programs governing meningeal biology.

Results

A *foxc1b*:Gal4 reporter marks developing meningeal populations in zebrafish

To assess whether the zebrafish paralogs for Foxc1 (*foxc1a* and *foxc1b*) are active in meninges, we examined zebrafish carrying the *foxc1b*:Gal4;UAS:mCherryNTR transgene (Whitesell et al., 2019). In contrast to the previously described *foxc1b*:GFP reporter, which is broadly expressed throughout the face and craniofacial skeleton, mCherry fluorescence was restricted to regions surrounding the brain (**Fig. 1A**). Orthogonal sections revealed that mCherry and GFP signals were co-detected within a single cellular layer positioned adjacent to the brain surface. Co-imaging with the epithelial marker *cdh1*:mlanYFP confirmed that mCherry^{+} cells reside beneath

the epithelium (**Fig. 1B**). To assess mesenchymal identity, *foxc1b*:Gal4;UAS:mCherryNTR fish were crossed with *fli1a*:GFP, a broad marker of craniofacial mesenchyme. mCherry$^+$ cells encasing the brain co-expressed *fli1a*:GFP, whereas *fli1a*:GFP-labeled vasculature lacked detectable mCherry signal (**Fig. 1C**). A developmental time course revealed no detectable mCherry signal at 24 hpf. By 36–48 hpf, mCherry$^+$/*fli1a*:GFP$^+$ cells emerged within the rostral meninges, while *fli1a*:GFP$^+$ cells appeared in caudal regions prior to mCherry detection. By 72 hpf, double-positive cells were broadly distributed around the brain (**Fig. 1D**). Time-lapse imaging confirmed early mCherry activation in the rostral meninges, primarily over the midbrain, with *fli1a*:GFP expression preceding mCherry in all regions (Movie 1). Together, these data define the spatiotemporal emergence of *foxc1b*$^+$ meningeal cells and establish *foxc1b*:Gal4 as a restricted reporter of meningeal development.

To further define the identity of mCherry$^+$ meningeal cells, we examined markers from the Daniocell single-cell transcriptomic dataset (Sur et al., 2023). Subsetting and reclustering of meningeal populations resolved two clusters of meningeal precursors, one cluster of meningeal fibroblasts, and three leptomeningeal clusters (**Fig. 1E**). Meningeal precursor clusters expressed canonical mesenchymal markers, including *fli1a* and *lum*, as well as the transcription factor *meox1* (**Fig. 1F**). Consistent with previous reports (Galanternik et al., 2025), all leptomeningeal clusters expressed ependymin (*epd*) and gamma-glutamylcyclotransferase b (*ggctb*), whereas the meningeal fibroblast cluster was distinguished by expression of solute carrier family 4 member 7 (*slc4a7*) and transferrin receptor protein 1a (*tfr1a*) (**Fig. 1F**). To validate these transcriptomic assignments in vivo, we performed RNAscope analysis, which confirmed expression of both *slc4a7* and *ggctb* transcripts within mCherry$^+$ meningeal cells by 5 dpf (**Fig. 1G**). These markers were frequently co-expressed and did not resolve into discrete layers, consistent with incomplete lineage commitment at larval stages.

Foxc1 paralogs exhibit conserved requirements during meningeal development

To test whether requirements for meningeal development are conserved across vertebrates, we examined the function of the transcription factors *foxc1a* and *foxc1b*, both of which were detected in meningeal precursor, meningeal fibroblast, and leptomeningeal populations (**Fig. 2A**). RNAscope analysis revealed co-expression of *foxc1a* and *foxc1b* in the rostral meninges by 36 hpf, including within mCherry$^+$ meningeal cells (**Fig. 2B**). Transcripts for both paralogs extended beyond the domain of mCherry expression, suggesting that reporter accumulation follows

132 *foxc1a*/*b* transcriptional activation. At this stage, mCherry^{+} meningeal cells were detected along
133 both the dorsal and ventral surfaces of the brain, whereas neither reporter nor *foxc1a*/*b* transcripts
134 were observed in the dorsal hindbrain or the most caudal ventral meninges. By 5 dpf, mCherry
135 and both foxc1 paralogs were broadly co-expressed throughout the meningeal layer encasing the
136 brain (**Fig. 2B**).
137
138 To determine the functional requirements of *foxc1a* and *foxc1b*, we generated an allelic series
139 using established mutant alleles (Xu et al., 2018) in combination with the
140 *foxc1b*:Gal4;UAS:mCherryNTR reporter. Loss of *foxc1b* alone did not alter meningeal reporter
141 distribution, as *foxc1a*$^{+/+}$; *foxc1b*$^{-/-}$ and *foxc1a*$^{+/-}$; *foxc1b*$^{-/-}$ larvae appeared phenotypically normal
142 (**Fig. 2C**). In contrast, loss of *foxc1a* resulted in reduced mCherry signal in the hindbrain
143 meninges, and removal of *foxc1b* in the *foxc1a* mutant background further exacerbated this
144 phenotype, consistent with a dosage-sensitive requirement for Foxc1 activity during meningeal
145 development (**Fig. 2C**).
146
147 Quantification of dorsal mCherry signal revealed regional differences in sensitivity to Foxc1
148 dosage (**Fig. 2D**). Midbrain meninges were comparatively resilient, with significant reductions in
149 mCherry signal detected only in *foxc1a*$^{-/-}$; *foxc1b*$^{+/-}$ and *foxc1a*$^{-/-}$; *foxc1b*$^{-/-}$ mutants. In contrast,
150 hindbrain meningeal signal was significantly reduced in *foxc1a*$^{-/-}$; *foxc1b*$^{+/+}$ larvae and further
151 diminished in *foxc1a*$^{-/-}$; *foxc1b*$^{+/-}$ mutants, with little additional loss upon complete *foxc1b*
152 removal. Spatiotemporal analysis demonstrated that reduced mCherry signal in *foxc1a*$^{-/-}$;
153 *foxc1b*$^{-/-}$ was evident by 36 hpf and persisted through 48 hpf and 72 hpf (**Fig. 2E**). Time-lapse
154 imaging confirmed that mCherry expression initiates rostrally over the midbrain but fails to expand
155 across the brain surface in mutant embryos (**Movie 2**).
156
157 To further resolve regional defects, mCherry^{+} meningeal cells were quantified across five dorsal–
158 ventral domains in sectioned larvae. While dorsal midbrain meninges were largely preserved in
159 *foxc1a*$^{-/-}$; *foxc1b*$^{-/-}$ mutants, all other regions exhibited significant depletion (**Fig. 2F,G**). To
160 assess meningeal integrity using additional markers, RNAscope was performed for the broad
161 meningeal marker *igfbp2a* and the leptomeningeal marker *ggctb*. In contrast to mCherry loss,
162 *igfbp2a* expression was maintained around the mutant brain, including in regions lacking
163 detectable mCherry signal (**Fig. 2H**). By comparison, *ggctb* expression was restricted to small
164 residual meningeal domains near the midbrain and was largely absent from the forebrain and
165 hindbrain, where mCherry loss was most pronounced (**Fig. 2H**). Together, these data

demonstrate a conserved, dosage-sensitive requirement for Foxc1 genes during vertebrate meningeal development and reveal region-specific dependence on Foxc1 activity across the developing brain.

Pharmacological inhibition identifies pathways required for meningeal formation

To identify developmental pathways required for meningeal establishment, we performed a targeted pharmacological screen using *foxc1b*:Gal4;UAS:mCherryNTR embryos. Inhibitors were applied beginning at 24 hpf, prior to mCherry$^+$ meningeal emergence, and embryos were analyzed at 72 hpf, when mCherry$^+$ cells normally encase the brain (**Fig. 3A**). Inhibition of Hedgehog (Cyclopamine), Notch (DAPT), retinoic acid (DEAB), FGF (Infigratinib), or TGFβ (LY2109761) signaling did not disrupt formation of a continuous meningeal layer (**Fig. 3B**). In contrast, inhibition of BMP signaling (Dorsomorphin) or Wnt signaling (XAV-939) prevented complete encasement of mCherry$^+$ meninges, with defects most pronounced in the dorsal hindbrain, the last meningeal population to form (**Fig. 3B**).

To determine whether early pathway inhibition was sufficient to disrupt meningeal development, embryos were transiently treated with XAV-939 or Dorsomorphin between 24 and 48 hpf and allowed to develop until 5–6 dpf (**Fig. 3C**). Treated larvae were comparable in size to controls but exhibited persistent depletion of mCherry signal within medial regions of the hindbrain meninges for both treatments (**Fig. 3D**). Analysis of *foxc1b*:Gal4;UAS:mCherryNTR; *fli1a*:GFP larvae revealed that mesenchymal cells persisted in the hindbrain following XAV-939 treatment, whereas mCherry reporter activation was selectively impaired. In contrast, Dorsomorphin-treated larvae lacked both mCherry and *fli1a*:GFP signal in this region, consistent with broader loss of mesenchymal cells (**Fig. 3D**).

XAV-939 treatment also appeared to impair forebrain meninges (**Fig. 3D**). To further assess this phenotype, we examined larvae carrying the forebrain meningeal reporter *tbx18*:dsRed2, which co-expresses with *foxc1b*:Gal4;UAS:nlsGFP (**Fig. 3E**). Transient XAV-939 treatment from 24 to 48 hpf resulted in a marked reduction of dsRed2 signal, particularly at the forebrain–midbrain boundary, indicating that Wnt signaling is required for proper establishment of forebrain meninges (**Fig. 3F**). Together, these data identify BMP and Wnt signaling as essential regulators of meningeal development and underscore the utility of zebrafish for dissecting conserved pathways governing formation of the vertebrate meninges.

200

201 **Adult zebrafish meninges are comprised of transcriptionally distinct fibroblasts**

202

203 During embryonic stages, zebrafish meninges appear as a single cellular (**Fig. 1G**), whereas prior
204 studies suggest that adult zebrafish meninges are multilayered (Galanternik et al., 2025). To
205 define the transcriptional identities of adult meningeal populations, we performed single-nucleus
206 multiomic profiling.

207

208 To assess persistence of *foxc1b* reporter expression in adults, brains and skullcaps were
209 dissected from *foxc1b*:Gal4;UAS:mCherryNTR fish. Robust mCherry signal was detected
210 surrounding the brain and along the ventral surface of the skullcap, with enrichment in midbrain
211 and hindbrain regions (**Fig. 4A**). RNA analysis confirmed co-expression of mCherry and *foxc1b*
212 in meninges associated with both brain and skull (**Fig. 4B**). Notably, pan-laminin immunostaining
213 selectively marked mCherry^{+} cells associated with the brain but not those adjacent to the skull,
214 suggesting molecular heterogeneity within adult meninges (**Fig. 4C**).

215

216 To define transcriptional and epigenetic profiles of adult meningeal populations, connective
217 tissues associated with the brain or skull were isolated from *foxc1b*:Gal4;UAS:nlsGFP and
218 *fli1a*:GFP fish, which we previously identified as labeling meningeal populations associated with
219 the calvaria (Farmer et al., 2024), and subjected to multiome analysis (**Fig. 4D**). After quality
220 control, 1,224 cells from the *fli1a*:GFP dataset and 1,188 cells from the *foxc1b*:Gal4;UAS:nlsGFP
221 dataset were recovered. Unsupervised clustering of merged datasets identified 17 distinct cell
222 populations that passed filtering (**Fig. 4E, Fig. S1A, Table S1**). Clusters included mesenchymal
223 populations expressing connective tissue markers such as *pdgfrb* and *col1a1a* (**Fig. S1B**), as well
224 as pericytes, smooth muscle/mural cells, endothelial cells, epithelial cells, immune populations,
225 pigment cells, and neuronal cell types (**Fig. 4E, Fig. S1C**). Relative abundance of non-
226 mesenchymal populations differed modestly between datasets, whereas endothelial, epithelial,
227 and T cell populations were present at comparable levels (**Fig. S1D)**.

228

229 Within mesenchymal populations, dermal fibroblasts were enriched in the *fli1a*:GFP dataset, while
230 *krt94*$^{+}$ mesenchymal cells, captured in our prior datasets (Farmer et al., 2024) and validated to
231 be a connective tissue that sits at the borders of skull (**Fig. S1E**), were preferentially enriched in
232 the *foxc1b*:Gal4;UAS:nlsGFP dataset (**Fig. 4F, G**). With the exception of a single cluster
233 (arachnoid fibroblasts), the remaining mesenchymal clusters exhibited comparable contributions

234 from both datasets (**Fig. 4F, G**). To further resolve the identities of previously uncharacterized
235 fibroblast populations, we analyzed cluster-enriched genes and assigned preliminary cell-type
236 identities, which we validate in this study. These populations include arachnoid fibroblasts, dural
237 fibroblasts, and two transcriptionally distinct periosteal dura fibroblast populations (**Fig. 4E-G**).
238
239 To relate zebrafish meningeal populations to mammalian counterparts, we reanalyzed published
240 mouse leptomeningeal and dura mater single-cell datasets (Pietila et al., 2023) and performed
241 cross-species comparisons. We identified genes enriched within each zebrafish cluster and
242 calculated module scores based on zebrafish genes and their mouse paralogs, enabling
243 systematic comparison across species (**Fig. S2A–D**). The *coch*$^{+}$ cluster corresponded most
244 closely to mouse pial fibroblasts and inner arachnoid cells (BFB1/BFB2), whereas the *slc6a2*$^{+}$
245 cluster matched a previously undescribed dura population enriched for *Pappa* (**Fig. S2E-F**). The
246 *ccn2a*$^{+}$ periosteal dura fibroblast cluster aligned with mouse outer dura populations expressing
247 *Matn4* and *Nppc* (Farmer et al., 2021) (**Fig. S2G**). In contrast, the *rspo2*$^{+}$ periosteal dura fibroblast
248 cluster lacked clear correspondence to known mouse meningeal populations (**Fig. S2H**).
249
250 Analysis of chromatin accessibility revealed cluster-specific regulatory programs. Arachnoid
251 fibroblasts were enriched for ETV, EGR, and GATA motifs, dural fibroblasts for TFAP, STAT, and
252 nuclear receptor motifs, and both populations for ZIC family motifs, consistent with known roles
253 in meningeal biology (Inoue et al., 2008) (**Fig. 4H**). Periosteal dura fibroblast clusters shared
254 enrichment for IRF, NFAT, and NFI motifs, while all meningeal populations exhibited enrichment
255 for ZNF family motifs, indicating distinct but overlapping regulatory architectures (**Fig. 4H**).
256
257 To spatially localize transcriptionally defined populations, RNAscope in situ hybridization was
258 performed in adult zebrafish. *ggctb*$^{+}$*igfbp2a*$^{+}$ cells persisted adjacent to the brain but were largely
259 absent beneath the skull, despite poor representation in single-cell datasets and co-expression
260 of *ggctb* and *foxc1b*:Gal4;UAS:GFP (**Fig. 5A; Fig. S3A**). Cells adjacent to the brain also
261 expressed transcripts encoding the secreted chemokine *cxcl12a* and the retinoic acid–
262 synthesizing enzyme *aldh1a2* (**Fig. S3B**). Arachnoid cells co-expressing *coch* and *igfbp2a* formed
263 a spatially discrete population restricted to brain-associated meninges and were positioned
264 superficial to *ggctb*$^{+}$ cells (**Fig. 5B,C**). In contrast, dural populations marked by *slc6a2* and
265 periosteal dura fibroblasts marked by *ccn2a* and *rspo2* localized preferentially to the skull-
266 associated side of the meninges **(Fig. 5D,E**). *ccn2a*$^{+}$ and *rspo2*$^{+}$ cells were intermingled within a

267 single bone-adjacent layer, consistent with transcriptionally distinct periosteal dura fibroblast
268 populations occupying the same anatomical compartment.
269
270 Together, these data demonstrate that adult zebrafish meninges comprise a multilayered and
271 transcriptionally heterogeneous structure consisting of at least four distinct populations: a pial
272 layer (*ggctb*$^+$*igfbp2a*$^+$), a discrete arachnoid layer (*coch*$^+$), an inner dura mater layer (*slc6a2*$^+$),
273 and a periosteal dura layer composed of intermingled *ccn2a*$^+$ and *rspo2*$^+$ fibroblasts (**Fig. 5F**).
274
275 **Larval meningeal ablation reveals long-term consequences on calvarial development**
276
277 To assess the functional requirement for the meninges during development, meningeal cells were
278 ablated using the *foxc1b*:Gal4;UAS:mCherryNTR line. Because ablation at juvenile or adult
279 stages resulted in lethality within 24 hours, subsequent analyses focused on larval ablation.
280 Larvae were treated with metronidazole (MTZ) or DMSO to induce apoptosis specifically in
281 mCherry$^+$ meningeal cells. MTZ treatment at 5 dpf resulted in widespread loss of mCherry signal,
282 confirming efficient meningeal ablation (**Fig. S4A,B**). Consistent with loss of meningeal integrity,
283 expression of the broad meningeal marker *igfbp2a* was markedly reduced around the brain at 0
284 and 1 days post-treatment (dpt), with discontinuous recovery by 2 dpt, indicating partial
285 regeneration of the meninges (**Fig. S4C**). MTZ-treated larvae exhibited reduced long-term
286 survival, with 54% surviving to 18 dpt compared to 87% of DMSO-treated controls, demonstrating
287 lasting consequences of larval meningeal ablation (**Fig. S4D**).
288
289 To examine long-term skeletal outcomes, MTZ-treated fish were raised to adulthood and their
290 craniofacial skeletons analyzed. Alizarin Red staining revealed widespread calvarial defects, with
291 the most prevalent phenotype consisting of a persistent opening in the skull (**Fig. 6A, B**). These
292 openings were frequently associated with misdirected bone growth, with bone folding on itself and
293 growing away from the opening (**Fig. 6B**). In addition, an ectopic bone occasionally formed
294 between the frontal and parietal bones (**Fig. 6B**). Defects were reproducibly localized to the
295 bregma, where cranial sutures converge (**Fig. 6C**).
296
297 To determine whether skeletal phenotypes were sensitive to the timing of meningeal ablation,
298 MTZ treatment was initiated at 3, 4, or 5 dpf. Ablation at 3 dpf, when the brain is already encased
299 by meninges, resulted in the lowest incidence of skeletal defects (~33%) (**Fig. 6D**). In contrast,
300 ablation at 4 or 5 dpf produced defects in ~80% of animals (**Fig. 6D**). Later ablation increased

both the frequency and size of calvarial openings and was associated with a higher incidence of ectopic bone formation (**Fig. 6E,F**). These findings indicate that meningeal disruption during larval stages causes persistent, stage-dependent defects in calvarial patterning.

To investigate the basis of calvarial openings, osteogenesis was examined during skull development. Prior to calvarial bone coverage, pigmented dura mater cells normally populate the juvenile head (Galanternik et al., 2025). In control animals at 8 mm, before calvarial bones encase the brain (Topczewska et al., 2016), these cells uniformly covered the midbrain and hindbrain (**Fig. 7A**). In contrast, MTZ-treated fish exhibited pronounced depletion of pigmented dura cells at the same stage, consistent with meningeal disruption preceding skull formation (**Fig. 7A**).

Repeated live imaging of *RUNX2*:EGFP fish revealed no differences between control and MTZ-treated animals at 9 mm, when calvarial bones have initiated growth but remain separated (**Fig. 7B**). However, by 14 mm, when bones normally approximate, MTZ-treated fish exhibited persistent openings at the prospective bregma. *RUNX2*$^{+}$ bone fronts failed to converge and instead appeared folded or misdirected, growing over adjacent bone. These defects persisted through 18 mm, a stage when cranial sutures are normally established, indicating failure of defect resolution. To determine whether osteoblast differentiation was impaired, the osteoblast:nlsEOS reporter was used to track de novo osteoblast formation (Farmer et al., 2024) (**Fig. 7C**). In control animals, newly differentiated osteoblasts accumulated as bone fronts approached and decreased after bones met (**Fig. 7D**). In contrast, MTZ-treated fish showed a marked reduction in de novo osteoblast differentiation at open bone fronts, with few newly differentiated osteoblasts detected near calvarial openings (**Fig. 7D, E**).

Given the reproducible localization of defects at the bregma, we tested whether localized meningeal ablation was sufficient to induce long-term craniofacial abnormalities. Targeted two-photon ablation of meningeal cells at the dorsal midbrain–hindbrain boundary resulted in efficient but transient loss of meningeal fluorescence, with robust regeneration by 30 hours post-ablation (**Fig. S5A**). Fish subjected to focal ablation and raised to adulthood exhibited no craniofacial abnormalities or calvarial openings (**Fig. S5B**). These findings indicate that large-scale, rather than localized, disruption of meningeal tissues is required to compromise calvarial development.

Impaired meninges regeneration leads to impaired calvarial and brain development

To define tissue-level disruptions underlying impaired osteogenesis and calvarial opening formation, histological and whole-mount analyses were performed on skulls from DMSO- and MTZ-treated animals. To preserve skull–brain architecture, zebrafish heads were plastic-embedded, sectioned, and stained with toluidine blue. In control samples, the brain remained closely apposed to the skull with intact intervening tissues (**Fig. 8A**). In contrast, MTZ-treated skulls failed to fully encase the brain, which instead adhered to the overlying dermis and exhibited disorganization of the underlying neural tissue (**Fig. 8A**).

To assess meningeal regeneration at sites of calvarial opening, RNAscope was performed on *foxc1b*:Gal4;UAS:mCherryNTR;UAS:GFP animals as mChery expression does not reactivate after MTZ treatment. In controls, GFP^+ meningeal cells lined the ventral skull surface and *igfbp2a*$^+$$GFP^+$ cells encased the brain (**Fig. 8B**). In MTZ-treated tissue, brain tissue remained adherent to the skin at calvarial openings, and neither GFP nor *igfbp2a* signal was detected at the defect itself, despite persistence of GFP^+ cells adjacent to surrounding bone and *igfbp2a*$^+$ GFP^+ around brain associated meninges away from the opening (**Fig. 8B**). These data indicate impaired meningeal regeneration at sites of failed bone formation.

Because some MTZ-treated skulls exhibited ectopic bone formation, meningeal regeneration was examined at these locations. RNAscope revealed irregular brain–skull adhesion and absent *igfbp2a* expression beneath ectopic bone, indicating that bone formation can occur in the absence of meningeal recovery but results in aberrant calvarial patterning (**Fig. S6**).

Consistent with histological and molecular analyses, imaging of the *wu:fj16a03*:nlsEOS reporter that labels brain-associated meningeal cells (**Fig. S7**), revealed depletion of EOS^+ cells overlying calvarial openings, with enrichment along the periphery of the defect on the skullcap (**Fig. 8C**). Single-cell transcriptomic analysis of DMSO- and MTZ-treated skullcaps showed largely comparable cellular compositions, with the exception of a cluster uniquely enriched in MTZ-treated samples expressing markers characteristic of arachnoid fibroblasts normally associated with brain meninges (**Fig. S8A-D**; **Tables S2**).

Transmission electron microscopy further confirmed loss of pigmentation and disorganization of fibroblast populations at calvarial openings, despite preservation of overlying dermal and epithelial structures (**Fig. S9**). Disruption of the underlying brain parenchyma was also observed, consistent with impaired meningeal support of neural tissue organization.

In control animals, bilateral optic tecta were clearly demarcated based on the distribution of *wu:fj16a03*:nlsEOS$^+$ cells, whereas this organization was lost in MTZ-treated brains (**Fig. 8C, arrows**). Whole-mount staining for acetylated tubulin confirmed disrupted brain architecture in regions lacking meningeal regeneration, including loss of proper separation between the optic tecta (**Fig. 8D**). Together, these findings demonstrate that impaired meningeal regeneration leads to persistent defects in both skull and brain development, underscoring the critical role of meninges in coordinating the organization and growth of adjacent tissues.

Discussion

The meninges have long been recognized as a critical connective tissue supporting and protecting the brain and skull (Dasgupta and Jeong, 2019), yet their cellular composition, developmental origins, and signaling functions remain incompletely understood. Here, we define the developmental emergence, molecular heterogeneity, and functional importance of zebrafish meningeal populations across larval and adult stages. By integrating genetic reporters, mutant analyses, single-cell multiomic profiling, spatial validation, pharmacological perturbation, and targeted ablation, we uncover conserved roles for the meninges in coordinating calvarial growth and brain organization.

Developmental emergence and heterogeneity of zebrafish meninges

Using a restricted *foxc1b*:Gal4 reporter, we show that zebrafish meningeal populations emerge in a spatiotemporally ordered manner, with rostral meninges forming before caudal populations, paralleling patterns described in mammals (Zarbalis et al., 2007). A notable distinction is the concurrent emergence of foxc1$^+$ meninges along both dorsal and ventral surfaces of the zebrafish brain, in contrast to predominantly basal initiation reported in mammals. During larval stages, meningeal cells exhibit incomplete lineage commitment, with co-expression of fibroblast and leptomeningeal markers within a single cellular layer, suggesting a prolonged plastic state. This may reflect delayed specialization in zebrafish that facilitates rapid growth and remodeling during early development.

In adults, single-cell profiling combined with spatial validation reveals a multilayered meningeal architecture composed of at least four transcriptionally and spatially distinct populations. These findings provide molecular resolution to prior anatomical descriptions (Galanternik et al., 2025)

403 and demonstrate that, as in mammals, zebrafish meninges comprise specialized layers with
404 distinct identities. Interestingly, although cells corresponding to each meningeal layer could be
405 identified based on positional and transcriptional features, certain specialized cell types, such as
406 arachnoid barrier and dural border cells, lacked clear zebrafish counterparts. This suggests that
407 zebrafish represent a simplified meningeal system, potentially accompanied by distinct structural
408 and functional differences compared with mammalian meninges. Nonetheless, the experimental
409 accessibility of zebrafish provides a powerful and tractable model for dissecting the core
410 mechanisms that govern meningeal stratification and layer-specific functions.
411
412 *Conserved regulatory programs governing meningeal development*
413 Functional analyses demonstrate a conserved, dosage-sensitive requirement for Foxc1 during
414 meningeal development, with region-specific dependencies across the brain. Loss of *foxc1a*
415 preferentially affects hindbrain meninges, while combined reduction of *foxc1a* and *foxc1b*
416 exacerbates defects, consistent with mammalian studies linking FOXC1 dosage to meningeal
417 integrity (Aldinger et al., 2009; Siegenthaler et al., 2009; Zarbalis et al., 2007). Interestingly,
418 although both paralogs show comparable expression during meningeal development, foxc1a
419 appears more critical, suggesting limited paralog-specific functions. Persistence of some
420 meningeal populations in Foxc1-deficient contexts suggests that additional transcriptional
421 regulators contribute to early meningeal specification.
422
423 Pharmacological perturbation identifies BMP and Wnt signaling as essential for meningeal
424 establishment, particularly for late-forming hindbrain populations. Disruption of Wnt signaling
425 selectively impaired meningeal differentiation without broadly affecting mesenchymal survival,
426 suggesting stage- or region-specific roles. These findings are consistent with prior work
427 implicating Wnt signaling in meningeal expansion (Choe et al., 2014) and highlight conserved
428 signaling pathways regulating meningeal development. Motif enrichment analyses further
429 implicate transcription factor families previously associated with meningeal biology, including ZIC
430 factors, suggesting that layered combinations of signaling inputs and transcriptional programs
431 generate meningeal diversity. The identification of population-specific enrichment of GATA,
432 TFAP, and NFAT motifs highlights new potential regulatory pathways for future study.
433
434 *Meninges as regulators of calvarial osteogenesis*
435 A central finding of this study is that meningeal integrity is required for proper calvarial bone
436 formation. Larval ablation of meninges results in persistent calvarial openings, misdirected bone

growth, ectopic bone formation, and defects localized to the bregma. These phenotypes are stage-dependent, with later ablation producing more severe defects, suggesting a progressive decline in meningeal regenerative capacity. Live imaging reveals that impaired calvarial development primarily reflects reduced de novo osteoblast differentiation at bone fronts rather than defects in initial bone specification. Notably, focal meningeal ablation is insufficient to induce long-term skeletal defects, indicating that large-scale or sustained disruption of meningeal tissue is required to compromise calvarial patterning. Together with the occurrence of ectopic bone formation in regions lacking canonical meningeal markers, these observations support a model in which meninges provide positional or organizational cues that support bone growth, rather than acting solely as inductive sources of osteogenic signals. Similar roles for meninges in maintaining suture patency have been described in mammals (Cooper et al., 2012; Greenwald et al., 2000; Kwan et al., 2008; Opperman et al., 1993; Slater et al., 2008), and hypomorphic *Foxc1* mutations produce calvarial openings reminiscent of those observed here (Zarbalis et al., 2007). It is possible that promiscuous adhesion of the meninges to adjacent tissues serves to re-establish a closed CSF system necessary for brain function, albeit at the expense of creating a suboptimal local environment for brain and bone.

Meningeal regeneration and tissue coordination

Despite partial regeneration following ablation, regenerated meninges fail to re-establish normal tissue architecture at calvarial openings. Loss of meningeal markers, abnormal brain–dermis adhesion, fibroblast disorganization, and disruption of underlying neural tissue correlate with defects in brain morphology, including impaired separation of the optic tecta. These findings underscore the role of meninges as both structural and signaling intermediates between the brain and skull.

Consistent with mouse studies, loss of meningeal tissue likely disrupts delivery of key secreted factors, such as retinoic acid (Como et al., 2025; Haushalter et al., 2017; Matrongolo et al., 2023; Mishra et al., 2016; Siegenthaler et al., 2009) and CXCL12 (Borrell and Marin, 2006), which regulate neural development and were also detected in zebrafish meninges adjacent to brain tissue. The pronounced brain phenotypes observed here highlight the conservation of meningeal–neural interactions and establish zebrafish as a powerful system for studying tissue coordination during craniofacial development.

Implications and future directions

Together, these findings position the meninges as dynamic, heterogeneous tissues essential for coordinating brain and skull development across multiple stages in zebrafish. Given the conservation of meningeal architecture and regulatory programs, insights from this model are likely to inform our understanding of human disorders influenced by meningeal-derived signals, including craniofacial disorders like craniosynostosis and calvarial dysplasia.

Figures and Figure Legends

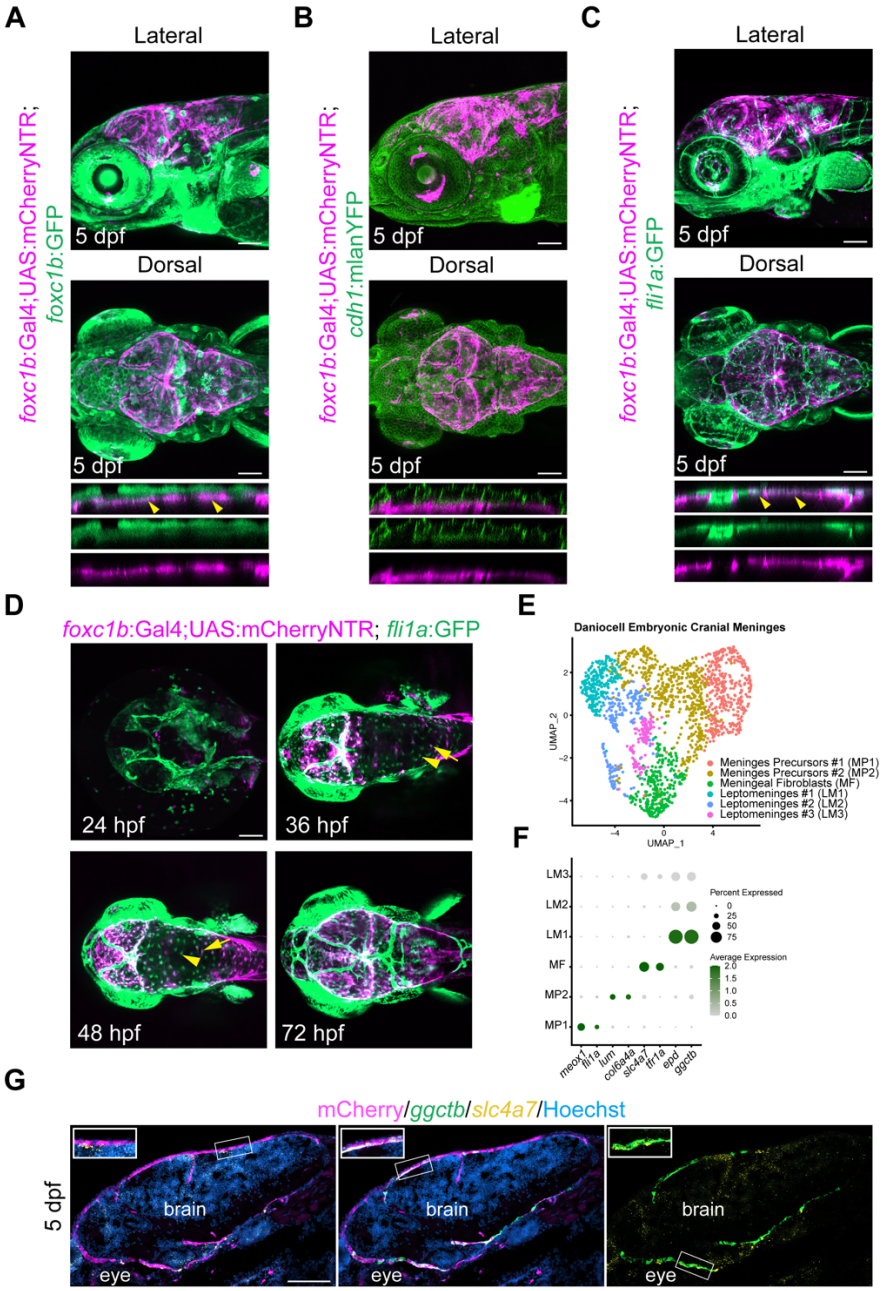

Figure 1. A *foxc1b* reporter specifically labels larval meninges and reveals early spatial patterns of meningeal formation. (A–C) Confocal images of 5 dpf zebrafish larvae showing detection of the *foxc1b*:Gal4;UAS:mCherryNTR reporter in combination with additional transgenic markers. Lateral (top) and dorsal (bottom) views are shown for each condition, with orthogonal sections provided to illustrate relative cell distribution (n=5 per condition). **(A)** Larvae carrying *foxc1b*:GFP together and *foxc1b*:Gal4;UAS:mCherryNTR show restricted mCherry^{+} expression

513 surrounding the brain, with GFP and mCherry co-expression enriched in cells closest to the brain
514 surface (arrowheads). **(B)** Co-imaging of *foxc1b*:Gal4;UAS:mCherryNTR with the epithelial
515 marker *cdh1*:mlanYFP shows non-overlapping expression. **(C)** Larvae carrying *fli1a*:GFP and
516 *foxc1b*:Gal4;UAS:mCherryNTR display co-expression of mCherry and GFP in cells surrounding
517 the brain. Arrowheads indicate representative double-positive cells. **(D)** Developmental time
518 course (24–72 hpf) of *fli1a*:GFP and *foxc1b*:Gal4;UAS:mCherryNTR expression. Arrows denote
519 $mCherry^{+}GFP^{+}$ cells, and arrowheads indicate GFP-only cells (n=5 per stage). **(E)** UMAP
520 clustering of subsetted meningeal populations from the Daniocell single-cell RNA-sequencing
521 dataset (Sur et al., 2023). **(F)** Dot plot showing marker genes enriched in each meningeal cluster
522 identified in (E). **(G)** In situ hybridization for leptomeningeal marker *ggctb* and meningeal fibroblast
523 marker *slc4a7*, combined with mCherry immunostaining in *foxc1b*:Gal4;UAS:mCherryNTR larvae.
524 Insets show higher-magnification views highlighting co-detection (n=3). Scale bars, 100 μM.

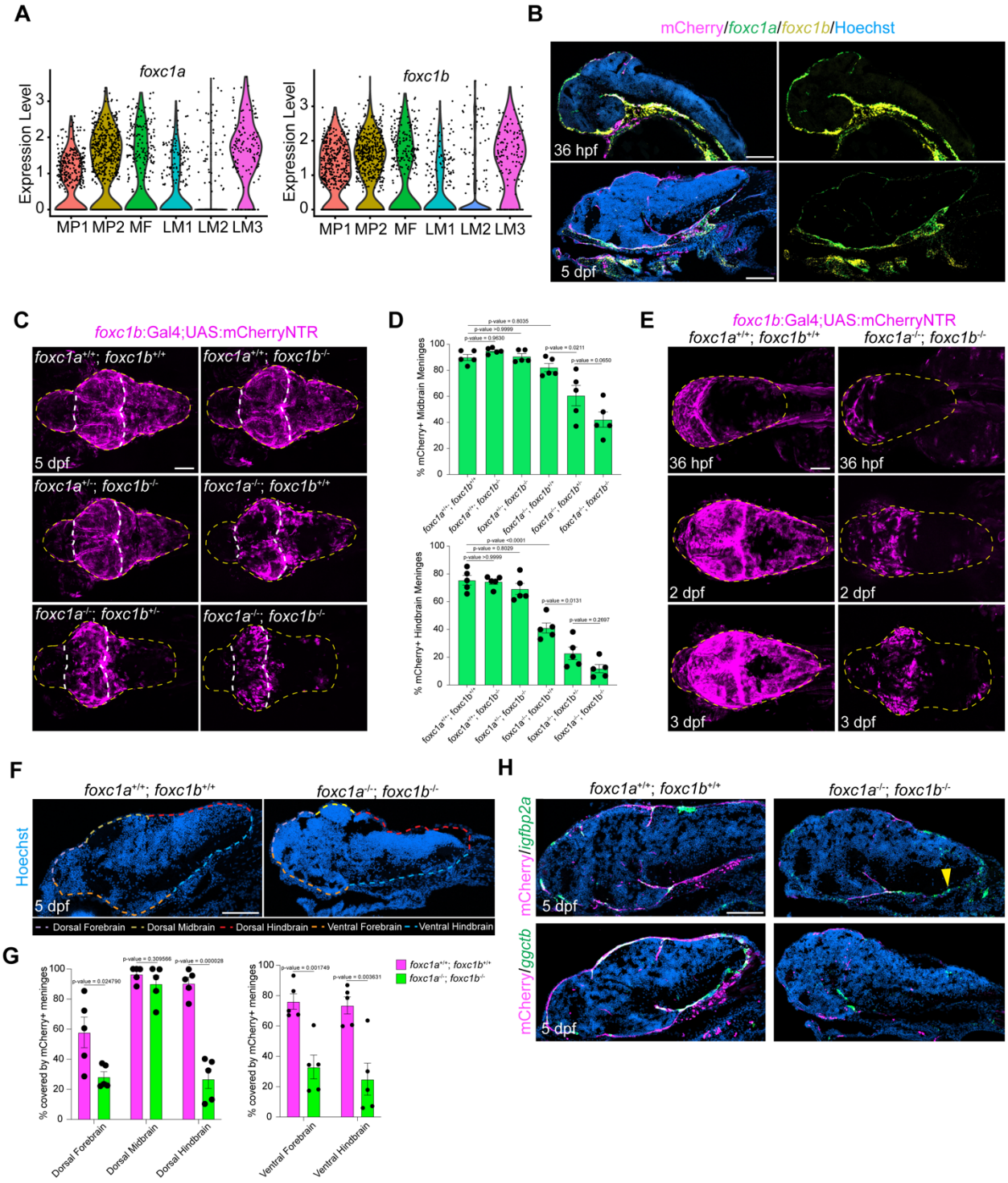

525

526 **Figure 2. *foxc1a* and *foxc1b* exhibit dosage-sensitive requirements for meningeal**
527 **formation. (A)** Violin plots showing expression of *foxc1a* and *foxc1b* across meningeal clusters.
528 **(B)** In situ hybridization for *foxc1a* and *foxc1b*, combined with mCherry immunostaining in
529 *foxc1b*:Gal4;UAS:mCherryNTR fish at 36 hpf and 5 dpf (n=3 per stage). **(C)** Dorsal-view confocal
530 images of *foxc1b*:Gal4;UAS:mCherryNTR larvae across an allelic series of *foxc1a* and *foxc1b*

531 mutants (n=5 per genotype). Yellow dotted lines outline the larval brain, and white dotted lines
532 demarcate the forebrain-midbrain and midbrain-hindbrain boundaries. **(D)** Quantification of dorsal
533 mCherry^{+} meningeal coverage of the midbrain and hindbrain across genotypes. **(E)**
534 Developmental time course (36 hpf–3 dpf) of *foxc1b*:Gal4;UAS:mCherryNTR expression in wild-
535 type and *foxc1a*$^{-/-}$; *foxc1b*$^{-/-}$ embryos (n=5 per genotype). Yellow dotted lines outline the larval
536 brain**. (F)** Representative histological sections of control and mutant larvae stained with Hoechst,
537 highlighting regions used for quantification of mCherry signal. Color coded dashed lines indicate
538 assigned zones for mCherry quantitation (n=5 per genotype). **(G)** Quantification of mCherry signal
539 surrounding the brain from histological sections shown in (F). **(H)** In situ hybridization for *igfbp2a*
540 or *ggctb*, combined with mCherry immunostaining in *foxc1b*:Gal4;UAS:mCherryNTR wildtype and
541 *foxc1a*$^{-/-}$; *foxc1b*$^{-/-}$ larvae (n=3 per genotype). Arrowhead marks *igfpb2a*$^{+}$ region devoid of
542 mCherry signal in mutant. P-values were calculated using two-tailed non-parametric Student's t-
543 tests. Error bars represent s.e.m. Scale bars, 100 μm.

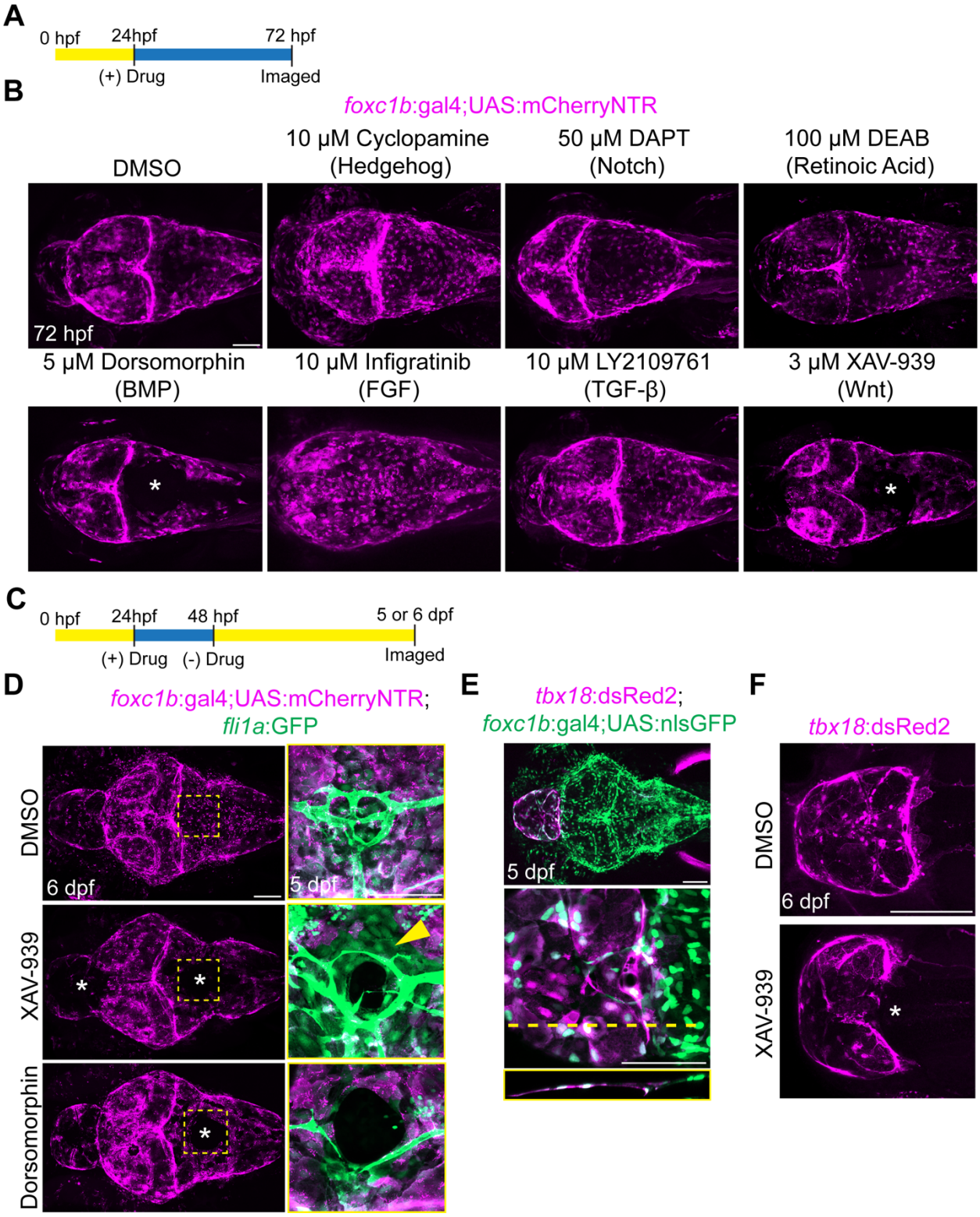

Figure 3. Drug screening of developmental pathways reveals a requirement for Wnt and BMP signaling during meningeal formation. (A) Schematic illustrating the short-term drug treatment strategy. **(B)** Dorsal-view confocal images of *foxc1b*:Gal4;UAS:mCherryNTR embryos

548 treated with inhibitors of developmental signaling pathways using the long-term drug treatment
549 paradigm and imaged at 72 hpf. Asterisks indicate reduced mCherry signal following
550 Dorsomorphin and XAV-939 treatment (n = 10 embryos per condition). **(C)** Schematic illustrating
551 the short-term drug treatment strategy. **(D)** Dorsal-view confocal images of
552 *foxc1b*:Gal4;UAS:mCherryNTR larvae treated with DMSO, XAV-939 or Dorsomorphin using the
553 short-term drug treatment paradigm and imaged at 5 or 6 dpf (n = 10 larvae per condition).
554 Asterisk marks rostral regions where mCherry^{+} cells appear reduced. The dotted box marks a
555 representative region shown at higher magnification, including co-imaging with *fli1a*:GFP.
556 Arrowhead indicates region containing *fli1a*:GFP single-positive cells in XAV-939–treated
557 embryos. **(E)** Dorsal-view confocal images of 5 dpf zebrafish larvae showing
558 *foxc1b*:Gal4;UAS:nlsGFP expression in combination with *tbx18*:dsRed2 (n = 5 larvae). Dorsal
559 (top) and magnified (bottom) views are shown, with orthogonal sections illustrating co-expression
560 within the rostral meninges. Dotted lines indicate regions used for orthogonal sections. **(F)** Dorsal-
561 view confocal images of *tbx18*:dsRed2 larvae treated with DMSO or XAV-939 using the long-term
562 drug treatment paradigm and imaged at 6 dpf. Asterisk shows disruption of dsRed2^{+} cells at the
563 forebrain-midbrain interface (n = 5 larvae per condition). Scale bars, 100 μm.

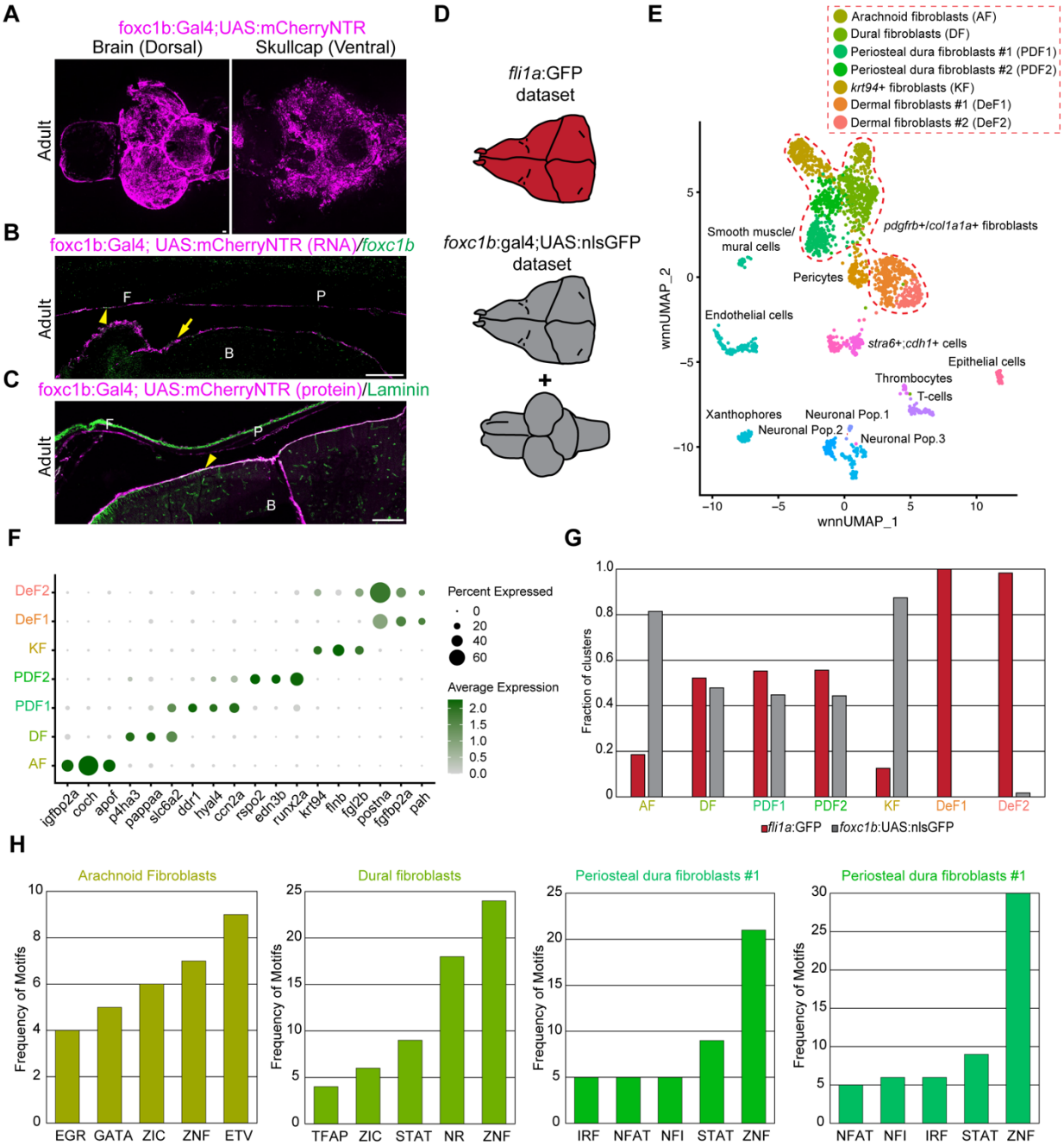

Figure 4. Single-cell genomics reveals multiple fibroblast cell types with zebrafish meninges. (A) Dorsal view of a dissected brain and ventral-view of a dissected skullcap from adult *foxc1b*:Gal4;UAS:mCherryNTR animals, showing mCherry expression associated with cranial meninges (n = 5). **(B)** In situ hybridization for *foxc1b* and mCherry in adult *foxc1b*:Gal4;UAS:mCherryNTR animals shows co-expression of *foxc1b* and mCherry in meningeal tissue located beneath the cranial bones (arrowhead) and surrounding the brain (arrow) (n = 3). **(C)** Immunostaining for laminin and mCherry in adult

572 *foxc1b*:Gal4;UAS:mCherryNTR animals shows co-detection in meninges surrounding the brain
573 (arrowhead) (n = 3). F= frontal bone, P= parietal bone, B= brain. **(D)** Schematic illustrating the
574 transgenic lines and tissues used for single-cell genomic experiments. **(E)** UMAP clustering of
575 sorted cells from merged datasets with cluster annotations. Red dashed lines delineate fibroblast
576 clusters, and predicted fibroblast identities are indicated within the dotted red box. **(F)** Dot plot
577 showing marker genes enriched in each fibroblast cluster identified in (E). **(G)** Graphical depiction
578 of the fraction of each fibroblast cluster captured from each dataset, with colors corresponding to
579 the schematic in (D). **(H)** Graphical depiction of the frequency of enriched transcription factor
580 family motifs within each representative cluster. Scale bars, 100 μm.
581
582
583
584
585
586
587

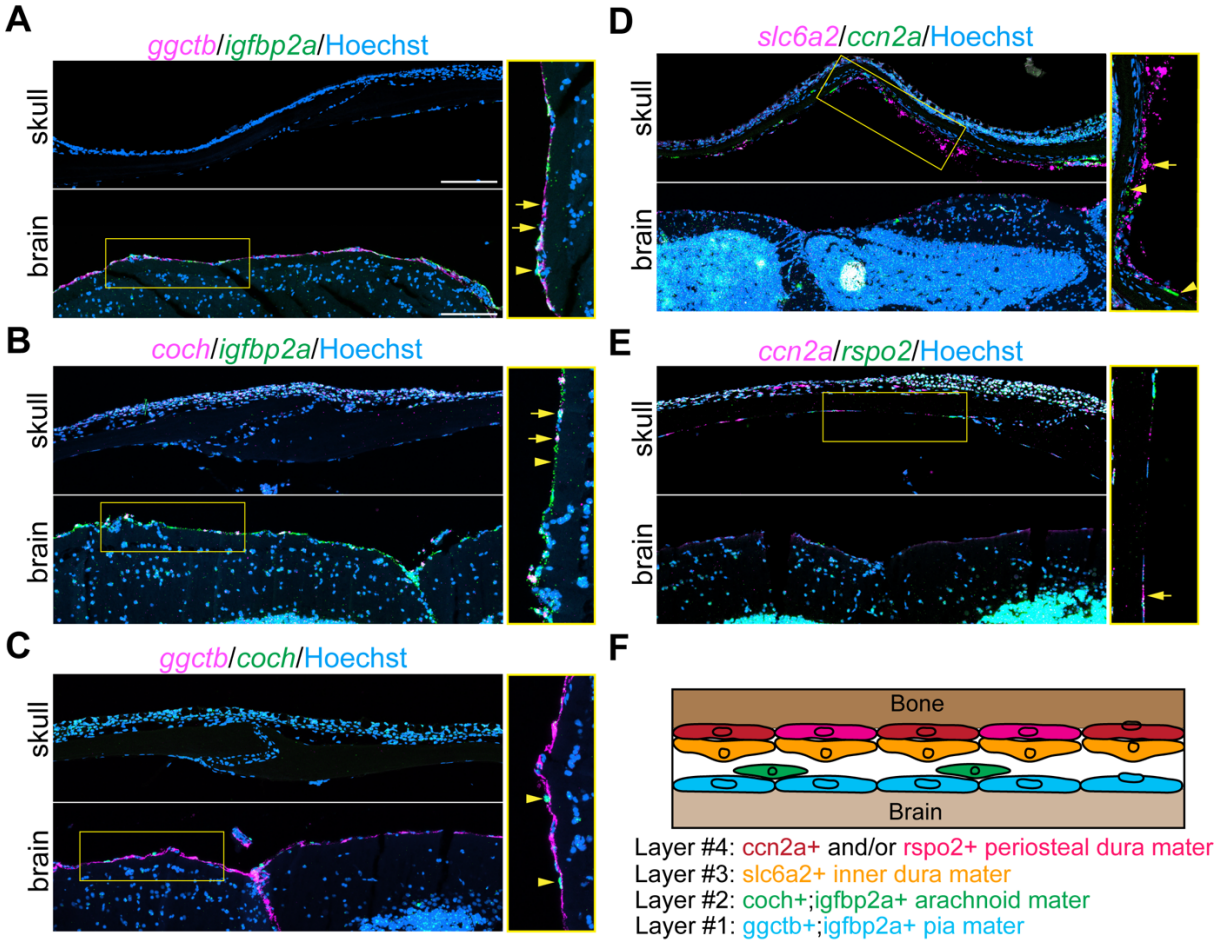

Figure 5. Meningeal fibroblasts are spatially organized into distinct layers between the skull and brain in the adult zebrafish. (A) In situ hybridization for *ggctb* and *igfbp2a* shows co-expression of both genes in cells surrounding the brain (arrows), with *igfbp2a*$^{+}$ cells (arrowhead) interspersed among double-positive cells. **(B)** In situ hybridization for *coch* and *igfbp2a* shows scattered co-expression of both genes around the brain (arrows), along with *igfbp2a*$^{+}$ cells (arrowhead) distributed along the brain surface. **(C)** In situ hybridization for *ggctb* and *coch* reveals non-overlapping expression domains, with *coch*$^{+}$ cells (arrowheads) positioned superficial to *ggctb*$^{+}$ cells. **(D)** In situ hybridization for *slc6a2* and *ccn2a* shows *ccn2a*^{high} cells (arrowheads) located closest to the bone, while *slc6a2*^{high} cells (arrows) are positioned farther from the bone. Low levels of *slc6a2* expression are also detected around the brain. **(E)** In situ hybridization for *ccn2a* and *rspo2* shows expression of both genes within the same layer adjacent to the bone, with double-positive cells (arrow) distributed along the skull. Signal for both genes is absent around the brain. **(F)** Model illustrating the spatial organization of meningeal subtypes within the adult zebrafish skull. Boxes indicate magnified regions corresponding to locations highlighted in the images. All stains were performed in biological triplicates.

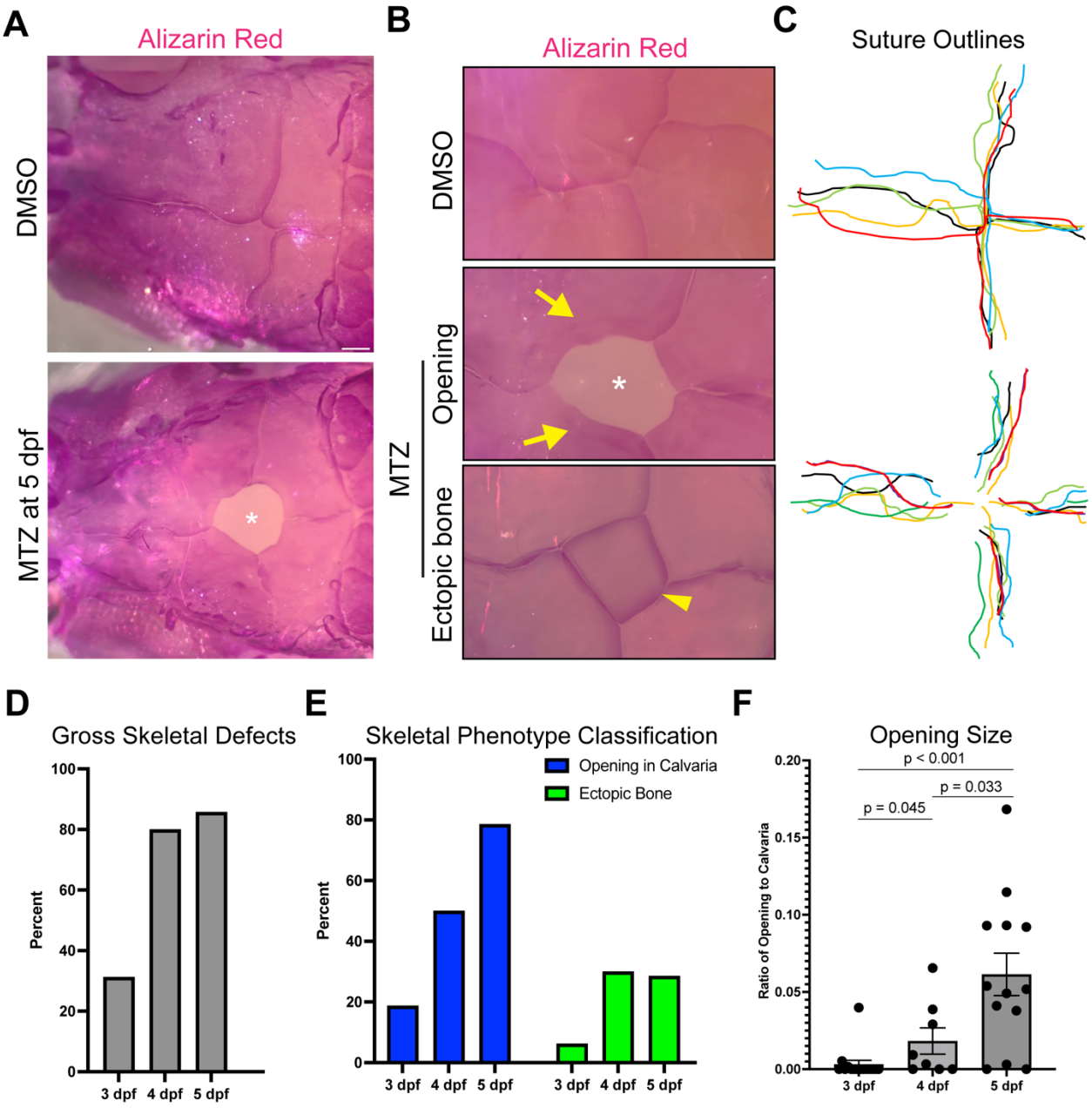

Figure 6. Larval ablation of meninges leads to persistent calvarial defects. (A) Dorsal views of Alizarin-stained skulls from DMSO- and MTZ-treated adult zebrafish reveal openings in the calvaria of treated fish (n = 13 fish per condition). **(B)** Representative images of the bregma region in Alizarin-stained skulls from DMSO- and MTZ-treated fish show a range of skeletal phenotypes in treated animals. Arrows indicate irregular lines around bones, suggestive of misdirected bone growth. Arrowhead indicated ectopic bone. Asterisks mark sites of calvarial openings **(C)** Hand-drawn outlines of suture borders in control and MTZ-treated zebrafish reveal reproducible defects at the bregma. **(D)** Quantification of MTZ-treated zebrafish exhibiting skeletal defects following ablation at different developmental time points. **(E)** Quantification of skeletal phenotype classes

614 observed at different treatment times. **(F)** Quantification of open calvarial defects expressed as
615 the ratio of opening area to total calvarial area. P-values were calculated using two-tailed non-
616 parametric Student's t-tests. Error bars represent s.e.m. Scale bars, 100 μm.
617

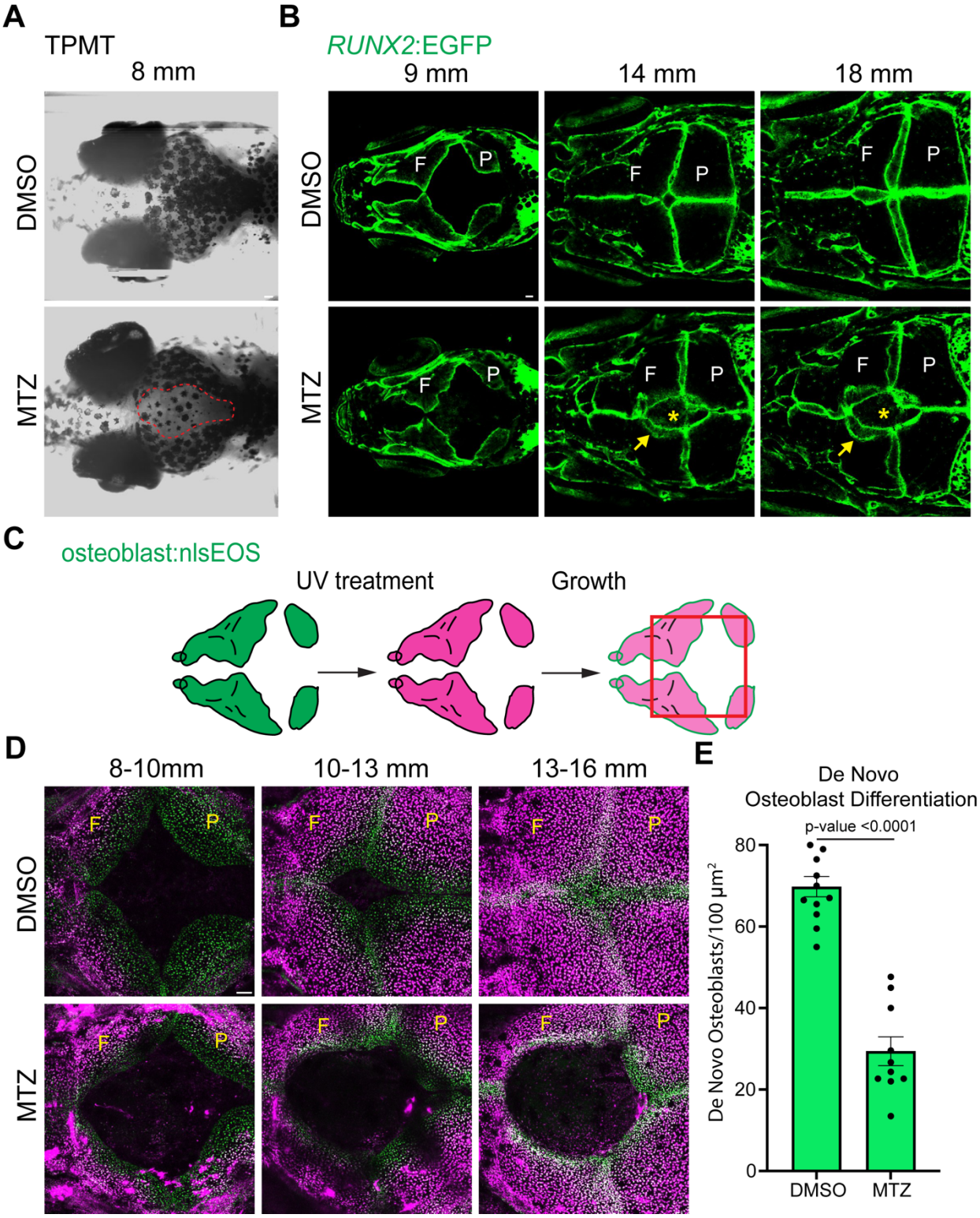

618

619 **Figure 7. Osteogenesis is disrupted by early ablation of meninges. (A)** Transmitted light
620 images of control- and MTZ-treated zebrafish at 8 mm (n = 5 fish per condition). The dotted line
621 demarcates the region of pigment depletion. **(B)** Dorsal-view confocal images from serial imaging

of *foxc1b*:Gal4;UAS:mCherryNTR; *RUNX2*:GFP zebrafish treated with DMSO or MTZ between 9 mm and 18 mm (n = 6 fish per condition). Arrows indicate regions of abnormal overlapping bone, and asterisks mark RUNX2-negative openings in the calvaria. **(C)** Schematic illustrating the treatment and imaging scheme used to quantify de novo osteoblast rates in the juvenile calvaria. The red box indicates the region imaged in subsequent panels. **(D)** Serial confocal imaging of individual DMSO- and MTZ-treated fish carrying the osteoblast:nlsEOS transgene shows reduced generation of de novo osteoblasts in treated animals. The same fish were photoconverted at approximately 8 mm and imaged at 10 mm, photoconverted again and imaged at 13 mm, photoconverted a final time and imaged at 16 mm (n = 5 fish per condition). F= frontal bone, P= parietal bone **(E)** Quantification of de novo osteoblasts at bone fronts.. P-values were calculated using two-tailed non-parametric Student's t-tests. Error bars represent s.e.m. Scale bars, 100 μm.

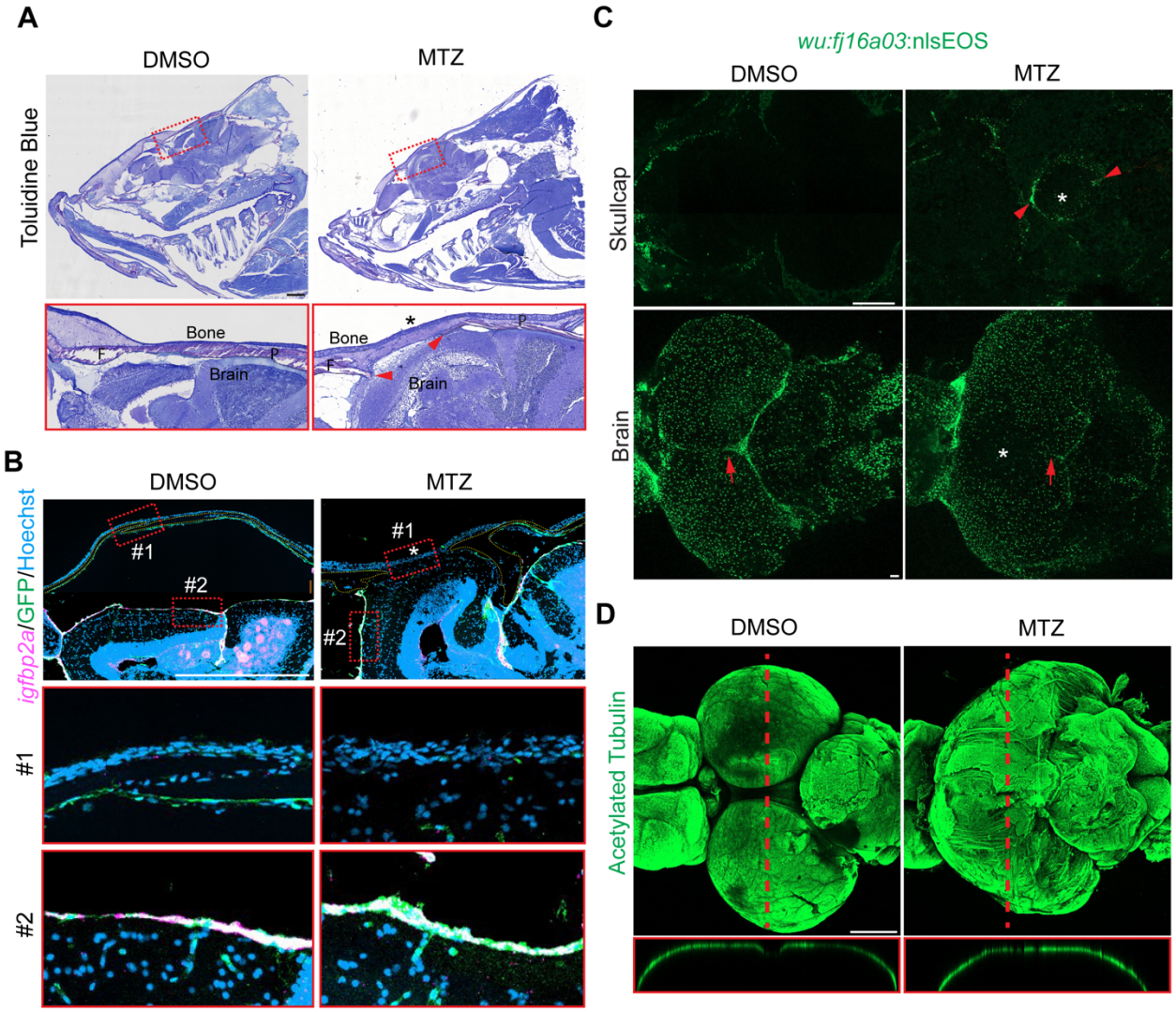

Figure 8. Fish fail to regenerate dorsal meninges, resulting in irregular skeletal and brain morphology. (A) Toluidine blue staining of plastic-embedded heads from DMSO- and MTZ-treated fish shows absence of calvarial bone and abnormal attachment of the brain to the overlying dermis and skin in treated animals (n = 3 fish per condition). Dotted boxes indicate regions shown at higher magnification in the lower panels. Arrowheads mark bone ends in MTZ treated skull. **(B)** In situ hybridization for *igfbp2a* combined with GFP immunostaining in *foxc1b*:Gal4;UAS:mCherryNTR;UAS:GFP heads (n = 4 fish per condition). Numbered dotted boxes indicate regions shown at higher magnification in the lower panels. **(C)** Confocal imaging of dissected skullcaps and brains from DMSO- or MTZ-treated fish carrying the *wu:fj16a03*:nlsEOS reporter (n = 3 fish per condition). Arrowheads mark EOS^+ cells adhered to the skullcap. Arrows indicate EOS^+ signal between optic tecta. **(D)** Confocal imaging of whole brains stained for acetylated tubulin reveals irregular brain morphology in MTZ-treated fish (n = 3

fish per condition). Dotted lines indicate regions used for orthogonal sections. F= frontal bone, P= parietal bone. Asterisks mark sites of calvarial openings. Scale bars, 100 μm.

Movie 1. Time-lapse of embryo carrying *fli1a*:GFP and *foxc1b*:Gal4;UAS:mCherryNTR reporters, beginning at 24hpf and imaged for approximately 72 hours.

Movie 2. Time-lapse of *foxc1a*$^{-/-}$; *foxc1b*$^{-/-}$ embryo carrying *fli1a*:GFP and *foxc1b*:Gal4;UAS:mCherryNTR reporters, beginning at 24hpf and imaged for approximately 72 hours.

Methods

Zebrafish

All experiments were approved by the Institutional Animal Care and Use Committee at the University of California, Los Angeles (Protocol #ARC-2022-044). Published lines include Tg(*fli1a*:eGFP)^{y1} (Lawson and Weinstein, 2002), Tg(Hsa.*RUNX2*-Mmu.Fos:EGFP)^{zf259} (Kague et al., 2016), *Tg(-5.0kbfoxc1b:EGFP)*^{mw44} (Miesfeld and Link, 2014), *Tg(foxc1b:gal4FF)*^{ca72} (Whitesell et al., 2019), *cdh1-mlanYFP*^{xt17} (Cronan and Tobin, 2019), *Tg(tbx18:DsRed2)*^{pd22} (Kikuchi et al., 2011), *Tg(UAS:GFP)(Asakawa et al., 2008), Tg(UAS-NTR:mCherry)*^{C264} (Davison et al., 2007), *Tg(UAS:nlsGFP)*^{el609} (Barske et al., 2020), *osteoblast*:nlsEOS (Farmer et al., 2024), *foxc1a*^{el543} (Xu et al., 2018), and *foxc1b*^{el620} (Xu et al., 2018). One transgenic line was created using CRISPR/Cas9-based genomic integration of nlsEOS (Kimura et al., 2014; Thomas and Raible, 2019): wu:fj16a03 (guide RNAs targeting the upstream of the 5' UTR: 5′-AATGATGAAATATCTCTGCG-3). One-cell embryos were co-injected with guide RNAs (200 ng/μL), mbait guide RNA (200 ng/μL), IDT Cas9 protein (150 ng/μL), and a mbait-nlsEOS plasmid (20 ng/μL). Founders were identified by screening progeny for nlsEOS fluorescence.

Single nuclei isolation

Adult zebrafish skullcaps were dissected away (*foxc1b*:gal4;UAS:nlsGFP, *fli1a*:GFP and DMSO and MTZ-treated *foxc1b*:Gal4;UAS:mCherryNTR) and fluorescent meninges attached to the brain were scraped away (*foxc1b*:gal4; UAS:nlsGFP) in Ringer's solution. Tissue was mechanically minced with a razor and all tissue was transferred to a 1.5 mL tube for enzymatic dissociation (0.25% trypsin (Life Technologies, 15090-046), 1 mM EDTA, and 400 mg/mL Collagenase D (Sigma, 11088882001) in PBS). Tissue was incubated on a nutator at 28.5 °C for ~45 min and

682 the enzymatic reaction was stopped by adding 6X stop solution (6 mM CaCl2 and 30% fetal
683 bovine serum (FBS) in PBS). Cells were pelleted by centrifugation (300 g) at 4 °C and
684 resuspended in a final volume of 500 uL of 0.03% BSA in PBS. DAPI was added to resuspended
685 cells, and cells were fluorescence-activated cell sorted to isolate live cells that were DAPI negative
686 and GFP or mCherry positive for enrich for fibroblast populations or just DAPI negative cells for
687 DMSO/MTZ skullcaps. Single nuclei suspension was collected by following 10X Genomics nuclei
688 isolation protocol with low cell input for Multiome. FACS cells were pelleted for 15 min (300 rcf at
689 4°C) and incubated with lysis buffer for 90 s on ice. Isolated nuclei were washed by Wash buffer
690 and Nuclei buffer and checked for nuclear integrity with a fluorescence confocal microscope with
691 DAPI staining before use in library construction.
692
693 **Single cell-omic library construction, sequencing, and alignment**
694 Multi-omic libraries (*foxc1b*:gal4;UAS:nlsGFP and *fli1a*:GFP) of snATACseq and snRNAseq from
695 the same barcoded single nuclei were constructed per manufacturer's instructions (10X
696 Genomics, Chromium Next GEM Single Cell Multiome ATAC + Gene Expression). Single-Cell
697 RNA sequencing libraries (DMSO or MTZ-treated *foxc1b*:Gal4;UAS:mCherryNTR) were
698 constructed by 10X Genomics Chromium Single Cell 3′ Library and Gel Bead Kit v.2. To capture
699 accessible chromatin and transcripts from the same nuclei in Multiome, accessible chromatin and
700 polyadenylated mRNA from the same nuclei were pulled down and barcoded with the same
701 sequences within isolated GEMs to achieve single-nuclei separation. cDNAs were synthesized
702 through reverse transcription from polyadenylated mRNA. Quality control of libraries was
703 assessed with the 4200 TapeStation system and Qubit dsDNA HS assay kit. Libraries were
704 sequenced on Illumina NovaSeq (Multiome) and NextSeq (scRNAseq) platforms. For Multiome
705 libraries, sequencing reads were aligned to customized genome built with GRCz11.fa,
706 GRCz11.104.gtf, and JASPAR2022.pfm with addition of GFP gene information and called peak
707 by Cell Ranger ARC v2.0.0 per manufacturer's instructions to generate peak-by-cell and gene-
708 by-cell count matrices. ScRNA-seq sequencing reads were aligned to customized genome built
709 from GRCz11 with addition of mCherry gene information by Cell Ranger v3.0.0 to generate gene-
710 by-cell count matrices.
711
712 **Single cell-omics data analysis**
713 scRNA-seq data using the 10X Genomics Chromium Single Cell 3′ Library and Gel Bead Kit v.2
714 was analyzed as previously described (Farmer et al., 2024). Multi-omics data were analyzed by
715 Seurat v5 and Signac v1.4 packages following the standard workflow with optimization. Cell

716 Ranger ARC-output count matrices of individual libraries were used to create Seurat objects by
717 “CreateSeuratObject” and “CreateChromatinAssay” functions. Quality control was performed by
718 setting the thresholds of accessible region counts (nCount_ATAC) < 40000 (foxc1b) or < 30000
719 (fli1a), transcript counts (nCount_RNA) < 6000 (foxc1b) or < 7500 (fli1a), ratio of
720 mononucleosome to nucleosome-free region (nucleosome_signal) < 3, and enrichment at TSS
721 (TSS.enrichment) > 0.5. In order to compare accessible chromatin regions (peaks) between
722 libraries, peaks-called were combined by “reduce” function that merges all intersecting peaks
723 between libraries and filtered by new peak widths (peakwidths < 10000 & > 20). The reduced-
724 peak list was used to recalculate peak-by-cell count matrices by “CreateFragmentObject”,
725 “FeatureMatrix”, and “CreateChromatinAssay” functions. “Merge” function was used to combine
726 count matrices of two libraries. Merged ATAC data were processed by “FindTopFeatures”
727 (min.cutoff = 5) and LSI linear dimension reduction; and merged RNA data were processed by
728 “SCTransform” and dimensionally reduced by PCA. 2:29 dimensions of LSI and 1:30 dimensions
729 of PCA were used to cluster cells with both ATAC and RNA information by
730 “FindMultiModalNeighbors” and “FindClusters” (resolution = 1, graph.name="wsnn", algorithm =
731 3). UMAP visualization was generated by “RunUMAP” (nn.name = "weighted.nn"). After filtering
732 for artificial clusters of dying cells , 19 clusters were identified. Differentially enriched genes were
733 calculated by “FindAllMarkers” (test.use = “wilcox”, logfc.threshold = 0.25, return.thresh = 0.01,
734 min.pct = 0.25). Differentially accessible regions were calculated by “FindAllMarkers” (test.use =
735 “LR”, logfc.threshold = 0.25, return.thresh = 0.01, min.pct = 0.1). To calculate motif enrichments
736 of each cell by chromVAR, “AddMotifs” was first used to calculate motif enrichments of each
737 accessible chromatin region (peak) followed by “RunChromVAR” to calculate motif activity in each
738 cell. “FindAllMarkers” test.use = “wilcox”, mean.fxn = rowMeans, logfc.threshold = 0.25,
739 return.thresh = 0.01, min.pct = 0.1) was performed to identify differentially enriched motifs.
740 Enriched motifs from the same family were grouped together to calculate the frequency of
741 enrichment for desired fibroblast clusters.
742
743 **Published dataset analysis**
744 The processed Seurat object and associated annotation list were downloaded directly from the
745 Daniocell website(Sur et al., 2023) and meninges clusters were subsetted and reclustered to
746 capture transcriptionally distinct clusters by refining the resolution. For mouse datasets, individual
747 leptomeningeal and dura mater datasets were downloaded from GEO and reanalyzed
748 independently using standard Seurat methods. Module scores were calculated using the
749 AddModuleScore function in Seurat with 10 control features. Scores were derived from 7–8 genes

750 differentially expressed in zebrafish meningeal clusters with clear mouse homologs. FeaturePlots
751 visualizing module scores were displayed with a minimum cutoff of the 10th percentile (q10) and
752 a maximum cutoff of the 90th percentile (q90).
753
754 **RNAscope in situ hybridization and immunofluorescence**
755 Embryonic and adult fish were measured and fixed individually in 4% PFA overnight at 4°C. Whole
756 embryos processed in 10% sucrose in PBS for one day and 30% sucrose in PBS for at least one
757 day before embedding tissue in Optimal Cutting Temperature (OCT) medium. Frozen sections
758 were cut at 10 µm. Adult heads were decalcified for 2 weeks and processed by paraffin embedding
759 as previously described (Farmer et al., 2024). RNAscope reagents were purchased from
760 Advanced Cell Diagnostics, and experiments were performed using the RNAscope Fluorescent
761 Multiplex V2 Assay according to the manufacturer's protocol for formalin-fixed paraffin-embedded
762 (adult) or for fixed frozen (embryos) sections. For cryosections, heat antigen retrieval was omitted.
763 The following probes were used for this study: Channel 1, dr-*gttcb*, dr-*krt94*, dr-*slc6a2,* dr-*foxc1b*;
764 Channel 2, dr-*coch*, dr-*foxc1a*, *mcherry*, dr-*slc4a7*; Channel 3, dr-*ccn2a*, dr-*igfbp2a*; Channel 4,
765 dr-*rspo2*. RNAscope experiments were followed by immunofluorescence or performed
766 independently using the same antigen retrieval reagents as the RNAscope Fluorescent Multiplex
767 kit, and slides were blocked for 1 h in 10% (adult stains) or 5% (embryonic stains) goat serum,
768 stained with primary overnight (anti-laminin, 1:250, Millipore #L9393; anti-GFP, 1:1000, Novus
769 NB100-1614; anti-mCherry, 1:1000, Novus NBP2-25157) and stained with Alexa-Fluor
770 secondaries from Thermo Scientific (1:250, Thermo) and Hoechst 33342 at room temperature for
771 1 h. Wholemount staining of adult brains were performed by permeabilizing tissues with 0.25%
772 Triton for 3 hours at room temperature followed by blocking in anti-acetylated α-tubulin antibody
773 (1:500, Sigma T6793) overnight, and the secondary for two hours at room temperature with
774 secondary antibody and Hoechst 33342.
775
776 **Transmission Electron Microscopy**
777 Whole heads were fixed with 2.5% glutaraldehyde and 4% paraformaldehyde in 0.1M sodium
778 cacodylate buffer overnight at 4°C, and decalcified for 2 weeks in 0.5 M EDTA. The hole area was
779 dissected away, including surrounding calvaria tissue and underlying brain. Dissected tissues
780 were then post-fixed in 1% osmium tetroxide in 0.1M sodium cacodylate or 0.1M PB, and
781 dehydrated through a graded series of ethanol concentrations. After infiltration with Eponate 12
782 resin, the samples were embedded in fresh Eponate 12 resin and polymerized at 60°C for 48
783 hours. Ultrathin sections of 70 nm thickness were prepared and placed on formvar/Carbon coated

copper grids and stained with uranyl acetate and Reynolds' lead citrate. The grids were examined using a JEOL 100CX transmission electron microscope at 60 kV and images were captured by an AMT digital camera (Advanced Microscopy Techniques Corporation, model XR611) (Electron Microscopy Core Facility, UCLA Brain Research Institute).

Plastic embedding

Zebrafish heads were dissected and fixed in 70% ethanol without decalcification. After dehydration, samples were gradually infiltrated with increasing concentrations of methyl methacrylate resin and embedded in 2.5% methyl methacrylate. Longitudinal sections (5 μm thick) were obtained using a Polycut microtome fitted with a tungsten carbide knife and stained with toluidine blue for histological analysis. Sections were subsequently stained with Toluidine Blue staining and imaged using an ECHO Revolution microscope.

2-photon ablation

5 dpf larvae were mounted in low-melting-point agarose and imaged on an inverted LSM 880 microscope equipped with a two-photon laser. Using a 20× air objective, a region at the midbrain–hindbrain boundary was manually delineated using the ROI tool to encompass approximately 20 nuclei. Targeted ablation was performed at 450 mW with a scan speed of 400 Hz for a total duration of 9 s (three cycles of 3 s each). Ablation efficacy was assessed by imaging in the transmitted photomultiplier tube (T-PMT) channel to confirm loss of pigmented cells. Z-stacks were acquired immediately after ablation and again 6 h post-treatment to verify sustained signal loss. Following imaging, larvae were individually housed and re-imaged at 1 and 2 days post-treatment (dpt) before being raised to adulthood.

Adult skeletal preparations

Skeletal preparations were performed as previously described (Teng et al., 2018), and zebrafish were imaged on a Zeiss Stemi with Zeiss Labscope software in 100% glycerol.

Imaging

All imaging was performed on a Zeiss LSM880 or a Zeiss LSM980 microscope using ZEN software. For repeated live imaging experiments, fish were anesthetized in Tricaine, mounted, and imaged using a 10X objective. For whole calvaria nlsEOS conversion experiments, live fish were transferred to a 6- or 12-well dish and exposed to a handheld UV light (UV Flashlight Black

817 Light, 3-in-1 Magnetic Flashlight Rechargeable, AdamStar) for 5–30 min. Converted fish were
818 individually housed and re-imaged for up to 2 months following initial conversion.
819
820 **Metronidazole treatment**
821 Zebrafish carrying *foxc1b*:gal4;UAS:mCherryNTR were outcrossed to wildtype AB zebrafish and
822 sorted by 5 dpf. mCherry+ fish were split into two groups to receive DMSO in Embryonic Media
823 (EM) or 10 mM Metronidazole in EM. Larvae were treated overnight and washed 3 times in EM
824 before entering the nursery at 6 dpf. Tanks for both conditions were assessed daily to assess
825 survival rate and imaged to confirm loss or return of fluorescence signal.
826
827 **Inhibitor drug screen**
828 Zebrafish embryos were screen for *foxc1b:*Gal4;UAS:mCherryNTR fluorescence at
829 approximately 18 hpf and chorions were digested enzymatically with 2 mg/mL Pronase. Fish
830 carrying *tbx18:*DsRed2 could not be screened before drug treatments. DAPT (Tocris, 2634), 4-
831 Diethylaminobenzaldehyde (Sigma-Aldrich, D86256), Dorsomorphin (Selleckchem S7840),
832 Infigratinib (Selleckchem, S2183), LY2109761 (Selleckchem, S2704), and XAV-939
833 (Selleckchem, S1180) were dissolved in DMSO and aliquoted as stock solutions. DAPT,
834 Infigratinib, and LY2109761 stock solutions were added to heated E3 and cooled to room
835 temperature before treating embryos. DEAB and Dorsomorphin stocks were diluted in room
836 temperature Embryo Medium. XAV-939 stock was added to heated Embryo Medium and cooled
837 to room temperature. Cyclopamine (Selleckchem S1146) was dissolved in Ethanol, and stock was
838 diluted into heated E3 and cooled to room temperature. PTU media was added to all drug
839 solutions, regardless of whether prepared in EM or E3, to a final concentration of 197 μM. Fresh
840 drug was added daily for animals treated from 24-72 hpf. For transient inhibition experiments,
841 drug media was replaced with 197 μM PTU in embryo medium every 24 hours until experiment
842 termination. Animals were euthanized and fixed in 4% PFA at 4ºC overnight prior to imaging.
843
844 **Quantification and statistical analysis**
845 For *foxc1a/*b allelic series, regions were defined by manually drawing ROIs around brain domains.
846 Fluorescent signal in the brain or deeper tissues was removed from the z-stack to avoid
847 misidentifying as dorsal meninges signal. Max projections of edited z-stacks were then
848 thresholded and measured for fraction of mCherry+ cells using ImageJ. For quantifying mCherry
849 expression around the perimeter of 5 dpf cryosections, brain domains and mCherry+ meninges
850 were manually defined in ImageJ by establishing ROI perimeters in ImageJ. For meninges

ablation experiments, entire calvaria were defined by manually drawing a ROI around the frontal and parietal bones using ImageJ. Hole regions were defined by manually drawing a ROI around the area where bone was absent in the calvaria. The measure tool was then used to obtain the areas of the entire calvaria and the hole regions in pixels. To quantify the size of each hole relative to the whole calvaria size, a ratio of hole area divided by entire calvaria area was calculated for each sample. For osteoblast:nlsEOS experiments, regions were defined by manually drawing a ROI across bone fronts or cranial sutures using ImageJ. The channels were then split and nuclei within each channel were counted manually. De novo osteoblasts were defined as green only cells. All statistical analyses were completed using PRISM.

Data availability

The raw and processed sequencing data for single-cell genomics datasets in this study are available on GEO (accession number: GSE318179).

Acknowledgements

The authors thank the Bone Histomorphometric Laboratory, the Brain Research Institute Microscopic Techniques and Electron Microscopy, and Broad Stem Cell Research Center's Flow Cytometry Core and Sequencing Core for their services. We thank you Susan Childs for providing the crucial *foxc1b*: Gal4;UAS:mCherryNTR fish line.

Contributions

A.L.A, K.W., H.C., and D.T.F conceived and designed the study. A.A. and B.M.H. performed larval experiments. K.W. and D.T.F. performed adult experiments. P.R. and K.W. generated and described the *wu:fj16a03*:nlsEOS reporter. H.C performed single-cell and bioinformatic analysis. D.T.F. supervised the research. D.T.F. wrote the manuscript with support from A.L.A, K.W., and H.C.

Funding:

HHMI Hanna H. Gray Fellows Program (D.T.F), HHMI Freeman Hrabowski Program (D.T.F.)

Competing interests

The authors have no competing interests to declare.

References

885 1. Aldinger, K.A., Lehmann, O.J., Hudgins, L., Chizhikov, V.V., Bassuk, A.G., Ades, L.C., Krantz, I.D.,
886 Dobyns, W.B., Millen, K.J., 2009. FOXC1 is required for normal cerebellar development and is a
887 major contributor to chromosome 6p25.3 Dandy-Walker malformation. Nat Genet 41, 1037-
888 1042.
889 2. Asakawa, K., Suster, M.L., Mizusawa, K., Nagayoshi, S., Kotani, T., Urasaki, A., Kishimoto, Y., Hibi,
890 M., Kawakami, K., 2008. Genetic dissection of neural circuits by Tol2 transposon-mediated Gal4
891 gene and enhancer trapping in zebrafish. Proc Natl Acad Sci U S A 105, 1255-1260.
892 3. Barske, L., Fabian, P., Hirschberger, C., Jandzik, D., Square, T., Xu, P., Nelson, N., Yu, H.V., Medeiros,
893 D.M., Gillis, J.A., Crump, J.G., 2020. Evolution of vertebrate gill covers via shifts in an ancient
894 Pou3f3 enhancer. Proc Natl Acad Sci U S A 117, 24876-24884.
895 4. Borrell, V., Marin, O., 2006. Meninges control tangential migration of hem-derived Cajal-Retzius
896 cells via CXCL12/CXCR4 signaling. Nat Neurosci 9, 1284-1293.
897 5. Choe, Y., Zarbalis, K.S., Pleasure, S.J., 2014. Neural crest-derived mesenchymal cells require Wnt
898 signaling for their development and drive invagination of the telencephalic midline. PLoS One 9,
899 e86025.
900 6. Como, C.N., Kim, S., Siegenthaler, J., 2023. Stuck on you: Meninges cellular crosstalk in
901 development. Curr Opin Neurobiol 79, 102676.
902 7. Como, C.N., O'Rourke, R., Winkler, C., Mitchell, D., Tran, L., Lorberbaum, D., Sussel, L., Franco, S.,
903 Siegenthaler, J., 2025. Meningeal-derived retinoic acid regulates neurogenesis via suppression
904 of Notch and Sox2. Cell Rep 44, 115637.
905 8. Cooper, G.M., Durham, E.L., Cray, J.J., Jr., Siegel, M.I., Losee, J.E., Mooney, M.P., 2012. Tissue
906 interactions between craniosynostotic dura mater and bone. J Craniofac Surg 23, 919-924.
907 9. Cronan, M.R., Tobin, D.M., 2019. Endogenous Tagging at the cdh1 Locus for Live Visualization of
908 E-Cadherin Dynamics. Zebrafish 16, 324-325.
909 10. Dasgupta, K., Jeong, J., 2019. Developmental biology of the meninges. Genesis 57, e23288.
910 11. Davison, J.M., Akitake, C.M., Goll, M.G., Rhee, J.M., Gosse, N., Baier, H., Halpern, M.E., Leach,
911 S.D., Parsons, M.J., 2007. Transactivation from Gal4-VP16 transgenic insertions for tissue-specific
912 cell labeling and ablation in zebrafish. Dev Biol 304, 811-824.

913 12. Decimo, I., Fumagalli, G., Berton, V., Krampera, M., Bifari, F., 2012. Meninges: from protective
914 membrane to stem cell niche. Am J Stem Cells 1, 92-105.
915 13. Derk, J., Como, C.N., Jones, H.E., Joyce, L.R., Kim, S., Spencer, B.L., Bonney, S., O'Rourke, R.,
916 Pawlikowski, B., Doran, K.S., Siegenthaler, J.A., 2023. Formation and function of the meningeal
917 arachnoid barrier around the developing mouse brain. Dev Cell 58, 635-644 e634.
918 14. DeSisto, J., O'Rourke, R., Jones, H.E., Pawlikowski, B., Malek, A.D., Bonney, S., Guimiot, F., Jones,
919 K.L., Siegenthaler, J.A., 2020. Single-Cell Transcriptomic Analyses of the Developing Meninges
920 Reveal Meningeal Fibroblast Diversity and Function. Dev Cell 54, 43-59 e44.
921 15. Ebert, S.N., Eisner, C., Karamboulas, K., Bernier, L.P., Kaplan, D.R., MacVicar, B.A., Miller, F.D.,
922 2025. Single-Cell Approaches Define the Murine Leptomeninges: Cortical Brain Interface as a
923 Distinct Cellular Neighborhood Composed of Neural and Non-neural Cell Types. eNeuro 12.
924 16. Farmer, D.T., Dukov, J.E., Chen, H.J., Arata, C., Hernandez-Trejo, J., Xu, P., Teng, C.S., Maxson, R.E.,
925 Crump, J.G., 2024. Cellular transitions during cranial suture establishment in zebrafish. Nat
926 Commun 15, 6948.
927 17. Farmer, D.T., Mlcochova, H., Zhou, Y., Koelling, N., Wang, G., Ashley, N., Bugacov, H., Chen, H.J.,
928 Parvez, R., Tseng, K.C., Merrill, A.E., Maxson, R.E., Jr., Wilkie, A.O.M., Crump, J.G., Twigg, S.R.F.,
929 2021. The developing mouse coronal suture at single-cell resolution. Nat Commun 12, 4797.
930 18. Galanternik, M.V., Castranova, D., Gober, R.D., Nguyen, T., Kenton, M., Margolin, G., Kraus, A.,
931 Sur, A., Dye, L.E., Pham, V., Maese, A., Holmgren, M., Gore, A.V., Samasa, B., Goldstein, A., Davis,
932 A.E., Swearer, A.A., Iben, J., Li, T., Coon, S.L., Dale, R.K., Farrell, J.A., Weinstein, B.M., 2025.
933 Anatomical and Molecular Characterization of the Zebrafish Meninges. bioRxiv.
934 19. Greenwald, J.A., Mehrara, B.J., Spector, J.A., Warren, S.M., Crisera, F.E., Fagenholz, P.J.,
935 Bouletreau, P.J., Longaker, M.T., 2000. Regional differentiation of cranial suture-associated dura
936 mater in vivo and in vitro: implications for suture fusion and patency. J Bone Miner Res 15, 2413-
937 2430.
938 20. Haushalter, C., Schuhbaur, B., Dolle, P., Rhinn, M., 2017. Meningeal retinoic acid contributes to
939 neocortical lamination and radial migration during mouse brain development. Biol Open 6, 148-
940 160.

941 21. Inoue, T., Ogawa, M., Mikoshiba, K., Aruga, J., 2008. Zic deficiency in the cortical marginal zone
942 and meninges results in cortical lamination defects resembling those in type II lissencephaly. J
943 Neurosci 28, 4712-4725.
944 22. Kague, E., Roy, P., Asselin, G., Hu, G., Simonet, J., Stanley, A., Albertson, C., Fisher, S., 2016.
945 Osterix/Sp7 limits cranial bone initiation sites and is required for formation of sutures. Dev Biol
946 413, 160-172.
947 23. Kappers, C.U.A., 1925. The meninges in Cyclostomes Selachians and teleosts compared with
948 those in man. P K Akad Wet-Amsterd 28, 72-80.
949 24. Kearns, N.A., Iatrou, A., Flood, D.J., De Tissera, S., Mullaney, Z.M., Xu, J., Gaiteri, C., Bennett, D.A.,
950 Wang, Y., 2023. Dissecting the human leptomeninges at single-cell resolution. Nat Commun 14,
951 7036.
952 25. Kikuchi, K., Gupta, V., Wang, J., Holdway, J.E., Wills, A.A., Fang, Y., Poss, K.D., 2011. tcf21+
953 epicardial cells adopt non-myocardial fates during zebrafish heart development and
954 regeneration. Development 138, 2895-2902.
955 26. Kimura, Y., Hisano, Y., Kawahara, A., Higashijima, S., 2014. Efficient generation of knock-in
956 transgenic zebrafish carrying reporter/driver genes by CRISPR/Cas9-mediated genome
957 engineering. Sci Rep 4, 6545.
958 27. Kwan, M.D., Wan, D.C., Wang, Z., Gupta, D.M., Slater, B.J., Longaker, M.T., 2008. Microarray
959 analysis of the role of regional dura mater in cranial suture fate. Plast Reconstr Surg 122, 389-
960 399.
961 28. Lawson, N.D., Weinstein, B.M., 2002. In vivo imaging of embryonic vascular development using
962 transgenic zebrafish. Dev Biol 248, 307-318.
963 29. Matrongolo, M.J., Ho-Nguyen, K.T., Jain, M., Ang, P.S., Reddy, A., Schaper, S., Tischfield, M.A.,
964 2023. Loss of Twist1 and balanced retinoic acid signaling from the meninges causes cortical
965 folding in mice. Development 150.
966 30. Miesfeld, J.B., Link, B.A., 2014. Establishment of transgenic lines to monitor and manipulate
967 Yap/Taz-Tead activity in zebrafish reveals both evolutionarily conserved and divergent functions
968 of the Hippo pathway. Mech Dev 133, 177-188.

969 31. Mishra, S., Choe, Y., Pleasure, S.J., Siegenthaler, J.A., 2016. Cerebrovascular defects in Foxc1
970 mutants correlate with aberrant WNT and VEGF-A pathways downstream of retinoic acid from
971 the meninges. Dev Biol 420, 148-165.
972 32. Nakao, T., 1979. Electron microscopic studies on the lamprey meninges. J Comp Neurol 183, 429-
973 453.
974 33. O'Rahilly, R., Muller, F., 1986. The meninges in human development. J Neuropathol Exp Neurol
975 45, 588-608.
976 34. Opperman, L.A., Sweeney, T.M., Redmon, J., Persing, J.A., Ogle, R.C., 1993. Tissue interactions
977 with underlying dura mater inhibit osseous obliteration of developing cranial sutures. Dev Dyn
978 198, 312-322.
979 35. Pietila, R., Del Gaudio, F., He, L., Vazquez-Liebanas, E., Vanlandewijck, M., Muhl, L., Mocci, G.,
980 Bjornholm, K.D., Lindblad, C., Fletcher-Sandersjoo, A., Svensson, M., Thelin, E.P., Liu, J., van
981 Voorden, A.J., Torres, M., Antila, S., Xin, L., Karlstrom, H., Storm-Mathisen, J., Bergersen, L.H.,
982 Moggio, A., Hansson, E.M., Ulvmar, M.H., Nilsson, P., Makinen, T., Andaloussi Mae, M., Alitalo,
983 K., Proulx, S.T., Engelhardt, B., McDonald, D.M., Lendahl, U., Andrae, J., Betsholtz, C., 2023.
984 Molecular anatomy of adult mouse leptomeninges. Neuron 111, 3745-3764 e3747.
985 36. Siegenthaler, J.A., Ashique, A.M., Zarbalis, K., Patterson, K.P., Hecht, J.H., Kane, M.A., Folias, A.E.,
986 Choe, Y., May, S.R., Kume, T., Napoli, J.L., Peterson, A.S., Pleasure, S.J., 2009. Retinoic acid from
987 the meninges regulates cortical neuron generation. Cell 139, 597-609.
988 37. Slater, B.J., Kwan, M.D., Gupta, D.M., Amasha, R.R., Wan, D.C., Longaker, M.T., 2008. Dissecting
989 the influence of regional dura mater on cranial suture biology. Plast Reconstr Surg 122, 77-84.
990 38. Slater, B.J., Kwan, M.D., Gupta, D.M., Lee, J.K., Longaker, M.T., 2009. The role of regional posterior
991 frontal dura mater in the overlying suture morphology. Plast Reconstr Surg 123, 463-469.
992 39. Sur, A., Wang, Y., Capar, P., Margolin, G., Prochaska, M.K., Farrell, J.A., 2023. Single-cell analysis
993 of shared signatures and transcriptional diversity during zebrafish development. Dev Cell 58,
994 3028-3047 e3012.
995 40. Teng, C.S., Ting, M.C., Farmer, D.T., Brockop, M., Maxson, R.E., Crump, J.G., 2018. Altered bone
996 growth dynamics prefigure craniosynostosis in a zebrafish model of Saethre-Chotzen syndrome.
997 Elife 7.

41. Thomas, E.D., Raible, D.W., 2019. Distinct progenitor populations mediate regeneration in the zebrafish lateral line. Elife 8.

42. Topczewska, J.M., Shoela, R.A., Tomaszewski, J.P., Mirmira, R.B., Gosain, A.K., 2016. The Morphogenesis of Cranial Sutures in Zebrafish. PLoS One 11, e0165775.

43. Whitesell, T.R., Chrystal, P.W., Ryu, J.R., Munsie, N., Grosse, A., French, C.R., Workentine, M.L., Li, R., Zhu, L.J., Waskiewicz, A., Lehmann, O.J., Lawson, N.D., Childs, S.J., 2019. foxc1 is required for embryonic head vascular smooth muscle differentiation in zebrafish. Dev Biol 453, 34-47.

44. Xu, P., Balczerski, B., Ciozda, A., Louie, K., Oralova, V., Huysseune, A., Crump, J.G., 2018. Fox proteins are modular competency factors for facial cartilage and tooth specification. Development 145.

45. Zarbalis, K., Siegenthaler, J.A., Choe, Y., May, S.R., Peterson, A.S., Pleasure, S.J., 2007. Cortical dysplasia and skull defects in mice with a Foxc1 allele reveal the role of meningeal differentiation in regulating cortical development. Proc Natl Acad Sci U S A 104, 14002-14007.